


NUREG/CR-2921  
SAND82-1145  
R7  
Printed March 1984

# Chemical Interactions of TELLURIUM Vapors With Reactor Materials

R. A. Sallach, C. J. Greenholt, A. R. Taig

Prepared by  
Sandia National Laboratories  
Albuquerque, New Mexico 87185 and Livermore, California 94550  
for the United States Department of Energy  
under Contract DE-AC04-76DP00789



8405220180 840430  
PDR NUREG  
CR-2021 R PDR

Prepared for  
**U. S. NUCLEAR REGULATORY COMMISSION**

**NOTICE**

This report was prepared as an account of work sponsored by an agency of the United States Government. Neither the United States Government nor any agency thereof, or any of their employees, makes any warranty, expressed or implied, or assumes any legal liability or responsibility for any third party's use, or the results of such use, of any information, apparatus product or process disclosed in this report, or represents that its use by such third party would not infringe privately owned rights.

Available from  
GPO Sales Program  
Division of Technical Information and Document Control  
U.S. Nuclear Regulatory Commission  
Washington, D.C. 20555

and  
National Technical Information Service  
Springfield, Virginia 22161

NUREG/CR-2921  
SAND82-1145

CHEMICAL INTERACTIONS OF TELLURIUM VAPORS  
WITH REACTOR MATERIALS

R. A. Sallach  
C. J. Greenholt  
A. R. Taig

Date Published  
March 1984

Sandia National Laboratories  
Albuquerque, New Mexico 87185

Operated by  
Sandia Corporation  
for the  
US Department of Energy

Prepared for the  
Division of Reactor Safety Research  
Office of Nuclear Regulatory Research  
US Nuclear Regulatory Commission  
Washington, DC 20555  
Under Memorandum of Understanding  
DOE40-550-75  
NRC FIN No. A1227

## ABSTRACT

The reaction of tellurium vapor with 304 stainless steel and Inconel-600 alloys in an as-received state and in a preoxidized state was studied for the temperature range 500°C to 800°C. Most reaction products were identified. The reaction is fast and appears largely limited by tellurium transport through the surrounding gas phase.

Also studied are the reactions of tellurium vapor with silver Zircaloy-2. Tellurium desorption rates from solid solutions of tellurium in nickel and 304 stainless steel were measured. The FLATDEP model for calculating tellurium deposition profiles is presented.



## TABLE OF CONTENTS

	<u>Page</u>
I. Introduction	1
II. Apparatus Procedures	2
III. Results and Discussion	5
A. Reaction With Unoxidized Alloys	5
B. Reaction With Preoxidized Alloys	12
C. Surface Reaction Kinetics--Application of FLATDEP Model	18
D. Desorption Measurements	19
IV. Summary	24
V. References	26
Appendix A -- FLATDEP Code	A-1
Appendix B -- Experimental Data	B-1

## LIST OF FIGURES

		<u>Page</u>
Figure 1.	Schematic Views of Experimental Apparati	3
Figure 2.	Appearance of Reacted Coupons Illustrating Typical Reaction Production Distributions	7
Figure 3.	Measured Mass Gains Versus Reciprocal Tellurium Reservoir Temperature	8
Figure 4.	Cross Section of 304 Stainless Steel Alloy Exposed to Tellurium Vapor	9
Figure 5.	Appearance of Silver Coupon After Exposure to Tellurium Vapor	11
Figure 6.	Elemental Distribution of a Cross Section of Zircaloy-2 Exposed to Tellurium Vapor	13
Figure 7.	Appearance of Preoxidized Coupons After Exposure to Tellurium Vapor	15
Figure 8.	Elemental Distribution of a Cross Section of Preoxidized 304 Stainless Steel After Exposure to Tellurium Vapor	17
Figure 9.	A Plot of Calculated Tellurium Deposition for Various Assumed Values of the Surface Reaction Rate Constant	20
Figure 10.	Desorption Rates of Tellurium for Tellurium-in-Nickel Solid Solution	22
Figure 11.	Desorption Rates of Tellurium for Tellurium-in-304 Stainless Steel Solid Solution	23
Figure A-1.	The Experimental System--as Modeled	A-3
Figure A-2.	Effect of $k_f$ on Deposition Profile	A-9
Figure A-3.	Axial Vapor Pressure Profiles--Surface Rate Constant = 0.01 m/s	A-10
Figure A-4.	Axial Vapor Pressure Profiles--Surface Rate Constant = 0.1 m/s	A-11
Figure A-5.	Axial Vapor Pressure Profiles--Surface Rate Constant = 1.0 m/s	A-12
Figure A-6.	Radial Vapor Pressure Profiles--Surface Rate Constant = 0.01 m/s	A-13

LIST OF FIGURES (Continued)

		<u>Page</u>
Figure A-7.	Radial Vapor Pressure Profiles--Surface Rate Constant = 0.1 m/s	A-14
Figure A-8.	Radial Vapor Pressure Profiles--Surface Rate Constant = 1.0 m/s	A-15
Figure A-9.	Effect of Gas Phase Tellurium Diffusion Coefficient on the Mass Transfer Limited Deposition Profiles	A-16
Figure A-10.	Effect of Assumed Plate Separation on the Mass Transfer Limited Deposition Profile	A-17
Figure A-11.	Tellurium Deposition Profiles Calculated Assuming a Four Fold Increase in Carrier Gas Flow Rate	A-18
Figure B-1.	Recorder Trace of a Microbalance Experiment	B-8
Figure B-2.	X-Ray Diffraction Pattern for Tellurium/Nickel Reaction Product	B-9
Figure B-3.	X-Ray Diffraction Pattern for Tellurium/Inconel-600 Reaction Product	B-10
Figure B-4.	X-Ray Diffraction Pattern for Tellurium/304 Stainless Steel Reaction Product	B-11
Figure B-5.	X-Ray Diffraction Pattern for Tellurium/Zircaloy-2 Reaction Product	B-12
Figure B-6.	X-Ray Diffraction Pattern for Tellurium/Oxidized Inconel-600 Reaction Product	B-13
Figure B-7.	X-Ray Diffraction Pattern for Tellurium/Oxidized 304 Stainless Steel Reaction Product	B-14

LIST OF TABLES

		<u>Page</u>
Table B-I	Experiment Data for Tellurium Adsorption (Reaction)	B-2
Table B-II	X-Ray Diffraction Data for Telluride Reaction Products	B-4
Table B-III	Data for Tellurium Desorption Experiments	B-7

## CHEMICAL INTERACTIONS OF TELLURIUM VAPORS WITH METAL ALLOYS

### I. Introduction

Shortly after the Three-Mile Island reactor accident, a program to investigate the vapor chemistry of fission products species released from degraded cores was started at Sandia National Laboratories. Its purpose was to identify the fission product species which would exist as vapors in the predominantly steam and hydrogen environment existing in the primary systems of Boiling Water Reactors and Pressurized Water Reactors and to explore the interactions of such fission product species with each other and with the structural materials of the primary system.

The more volatile fission product elements released from reactor fuel belong to these chemical families:

1. Rare gases--xenon and krypton
2. Halogens--iodine and bromine
3. Alkalies--cesium and rubidium
4. Chalcogens--tellurium and selenium

The inert gases, Xe and Kr, are nonreactive in these environments and their transport to containment and/or the surroundings cannot be modified or controlled by chemical means. The remaining elements are chemically active and their distribution and transport will be influenced by the chemical environment. When the fission product tellurium is introduced into steam/hydrogen mixtures the expected tellurium vapor species are  $Te_2$  or  $Te$ , although  $H_2Te$  can become significant when large hydrogen overpressures are present (Reference 2).

However, these vapor species of tellurium may not persist in the primary system since tellurides of nickel, iron, and chromium are stable to high temperatures. For this fission product then, there are good prospects for its retention in the reactor primary system by reaction with structure materials, largely 304 stainless steel and Inconel 600 alloys.

Prior investigations include measurements of the thermodynamic properties and determination of the phase diagrams for the Ni+Te, Fe+Te, and Cr+Te binary system by Komarek, et al (References 3, 4, 5). The role of tellurium in stress corrosion of cladding alloys was reported by Antill, et al (References 6, 7). Lobb and Robbins studied in detail the reaction of tellurium vapor with a 20 percent Cr/25 percent

Ni/Nb stabilized stainless steel (Reference 8) while the reaction of tellurium with 316 stainless steel and Zircaloy-4 was studied by Amand and Pruthi (Reference 9).

In this report, we present data obtained when  $\text{Te}_2$  vapor (in an argon carrier gas) reacted with 304 stainless steel and Inconel alloys. Two alloy states were studied: an unoxidized as-received state and a partially oxidized state. The reaction was followed by continuously measuring the specimen mass. Temperatures ranged between 773 K and 1273 K and the tellurium partial pressure ranged between 0.3 and 0.7 torr. Some reaction products were identified. Also included are data from a small number of experiments in which the interaction of tellurium with silver and with Zircaloy-2 was studied.

In addition, a computer code was developed to model the reaction. Variation of the parameters of this model permitted an "order of magnitude" characterization of the reaction rate between tellurium vapor and the various metals.

## II. Apparatus and Procedures

The measuring instrument used for both the absorption (reaction) and desorption experiments was a Cahn model R-100 Electrobalance. Coupon (sample) masses were 6 to 7 grams. Balance sensitivity (noise level) was limited to  $10^{-5}$  gram not by the balance characteristics but by building vibrations.

Two modifications of the apparatus were used, one for desorption and the other for absorption experiments. These modifications were concerned with the components reaching into the furnace which are detailed in Figure 1. They differ in how the carrier gas is introduced. In the desorption experiments, the carrier gas passed down into the furnace in a parallel tube to be injected at the bottom of the sample suspension tube. In absorption experiments, the carrier gas is introduced at the top of an annular section, passes down through the tellurium reservoir, then to the bottom of the inner suspension tube. In both modifications gas flows upward past the sample to meet a counter flow of gas from the balance chamber; both gas flows exit together through a side tube. The counter flow of gas ensures that the balance is never exposed to tellurium vapor or aerosol.

The quartz glass suspension tubes, 25 mm diameter and 510 mm length, have an inverted thermocouple well protruding from the bottom of the tube to within approximately 10 millimeters of the sample location. The type K thermocouple in this well is presumed to read the sample temperature. The carrier gas was research grade high purity tank argon; its control and flow measurement was made with Matheson ball-type rotameters. The samples were heated with a 16-inch Marshall



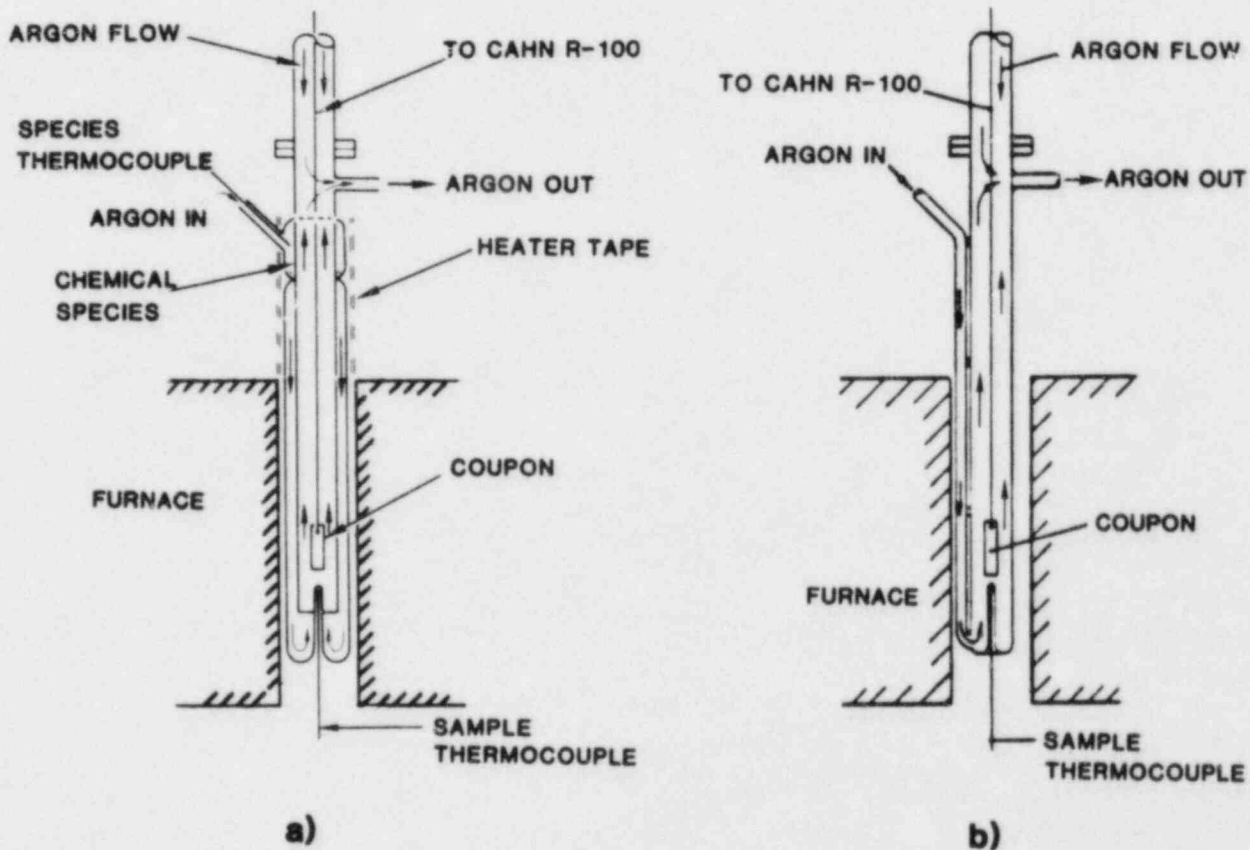


Figure 1. Schematic Views of Experimental Apparatus  
 a) Arrangement for absorption studies.  
 b) Arrangement for desorption studies.



tube furnace; the samples were located at the center of the furnace. Furnace temperature was controlled by a Leeds and Northrop controller (model XL-670). The tellurium reservoir of the absorption modification was heated with a heat cord (tape). Power to the cord was regulated by an Omega temperature controller (model 4001 KC).

The output of the Electrobalance was recorded on a Leeds and Northrup strip chart recorder and also displayed simultaneously on a digital voltmeter. The sample temperature, as measured by an Inconel sheathed Chromel-Alumel thermocouple was also recorded on the strip chart. Gas flow rates were set manually. The nominal flow was  $5.0 \times 10^{-2}$  liters/min measured at laboratory ambient conditions (295 K and 82.9 KPa). Some experiments were made at  $2.5 \times 10^{-2}$  and  $1.0 \times 10^{-1}$  liter/min. At the nominal flow of  $5.0 \times 10^{-2}$  liters/min, the average gas velocity past the coupon is calculated to be 0.45 cm/sec at 773 K and 0.62 cm/sec at 1073 K.

Elemental tellurium (Alpha Chemical Co., 99.5 percent), in the form of coarse powder, was spread throughout the annular reservoir and was supported by silica glass wool. The wool in turn was supported by a constriction in the outer glass wall. Perforce the argon carrier gas passes through the tellurium powder and the glass wool bed thereby establishing a partial pressure of tellurium vapor whose magnitude is determined by the reservoir temperature. The equation used to relate partial pressure and temperature is

$$\log_{10} P(\text{torr}) = 7.095 - \frac{5630}{T(\text{K})}$$

obtained by fitting the data of reference 10.

The generalized procedure used for the absorption studies is described below. For some tests, minor deviations in timing were made. Each alloy coupon was weighed on an analytical balance and its dimensions were measured. The alloy coupon was then suspended from the Cahn balance and sufficient tare mass was added to produce a balance output corresponding to several milligrams relative mass. After the suspension tube/tellurium reservoir was attached, an argon gas flow was started and the system was flushed overnight to displace any residual air. Final adjustments to gas flow rate were made and the recording of mass was started. The sample furnace was then heated to the desired experimental temperature. When the sample temperature had stabilized and the mass reading was again constant (buoyancy effects having caused small offsets of mass reading) the heat tape surrounding the tellurium reservoir was turned on. Approximately 5-10 minutes were needed to stabilize the tellurium reservoir temperature (there is low thermal inertia with the heat tape). The changing mass was recorded for 15 to

60 minutes in order to establish a good value of the rate of mass gain. The tellurium reservoir temperature was then changed to a new value and the new rate of mass gain was determined. This step was repeated until a range of experimental conditions had been investigated. After the coupon was removed from the apparatus, it was reweighed and the total mass increase was compared to the Cahn balance results. A typical recorder trace is shown in Appendix B.

This procedure is valid whenever there are no saturation effects, i.e., whenever diffusion processes in the solid reactants or products are not the rate-controlling steps. As shown later, this appears to be the case for experiments described in this report.

The argon carrier gas was purified by passage through hot zirconium metal turnings (1150 K to 1250 K); this process removes traces of oxygen, water vapor, and nitrogen. This purification stage was omitted when hydrogen was added to the carrier gas.

### III. Results and Discussion

We present first, the results of the tellurium reaction with the unoxidized alloys, then the results of the reaction of tellurium with the preoxidized alloys. Next is the brief description of the FLATDEP code and how it is applied to the tellurium reaction data. Last are the data for the desorption experiments.

#### A. Reaction With Unoxidized Alloys

A nonoxidizing condition (i.e., a low oxygen potential) is created by using as a carrier gas argon that had been purified by passage through hot zirconium metal turnings or argon to which hydrogen gas was added ( $\leq 10$  percent  $H_2$ ). Under these conditions the reaction of tellurium vapor with the alloys is the only measurable process. Thus, one would expect results consistent with the earlier data of Lobb and Robbins (Reference 8).

Our experimental data for unoxidized alloys are listed in Table B-1 of Appendix B. What we observe is:

- 1) the specimens gain mass at a linear rate--a constant amount per unit time,
- 2) this linear rate is proportional to the tellurium partial pressure,
- 3) the linear rate does not change as the temperature of the specimens is varied between 773 K and 1273 K, and lastly,

- 4) the reaction product is not distributed uniformly along the length of the specimens but is concentrated on the surfaces first exposed to the carrier gas stream.

Typical reaction product distributions for the alloys are shown in the photographs of Figure 2. Included also in the figure is the reaction product distribution for a pure nickel specimen.

From the above observations, one deduces that substantially all the  $\text{Te}_2$  vapor must have reacted with the metal alloys. There is good agreement (within 10 percent) between the measured rate of mass gain and the mass flow of tellurium calculated from the  $\text{Te}_2$  partial pressure and the carrier gas flow rate. This agreement is shown in Figure 3 in which the logarithm of the measured mass gain (at 0.05 l/min flow) is plotted against the reciprocal of the tellurium reservoir temperature (in Kelvins). The line is the calculated rate of tellurium transport at 0.5 l/min carrier gas flow. The reaction product distributions demonstrate that  $\text{Te}_2$  is rapidly removed from the carrier gas stream and imply as well that any solid state diffusion processes--whether of metal through the reaction product to the gas/solid interface or of tellurium through the reaction product to the metal/product interface--must also be rapid with respect to the incident flux of  $\text{Te}_2$  vapor to the specimen surface. Otherwise saturation effects would prevail resulting in both a more uniform distribution of reaction product and a nonlinear uptake of tellurium vapor.

The reaction products were identified from their x-ray diffraction patterns and are listed in Table B-II. Good correlations were found between the observed line intensities and the published data (Reference 11) implying that there were not preferred orientation in the reaction product layer. In contrast to Lobb and Robbins (Reference 8), we did not observe the formation of a duplex layer, but that may result from the generally shorter duration of our tests or alternately from the continuous nature of the telluriding process in the present experiment versus the reaction and annealing nature of their experiments. Representative cross sections are shown in Figure 4.

On 304 stainless steel,  $\text{Fe}_{2.25}\text{Te}_2$  is the major phase as would be expected, with  $\text{CrTe}$  present in lesser amounts commensurate with the chromium concentration in the alloy. No nickel tellurides were indicated by the x-ray diffraction pattern. It is probable that nickel has been incorporated into the  $\text{Fe}_{2.25}\text{Te}_2$  phase. On Inconel 600, the major phase is  $\text{Ni}_{2.86}\text{Te}_2$  with lesser amounts of  $\text{CrTe}$  present. No iron tellurides were indicated in the diffraction pattern. It is presumed that iron would have been incorporated into the  $\text{Ni}_{2.86}\text{Te}_2$  phase.

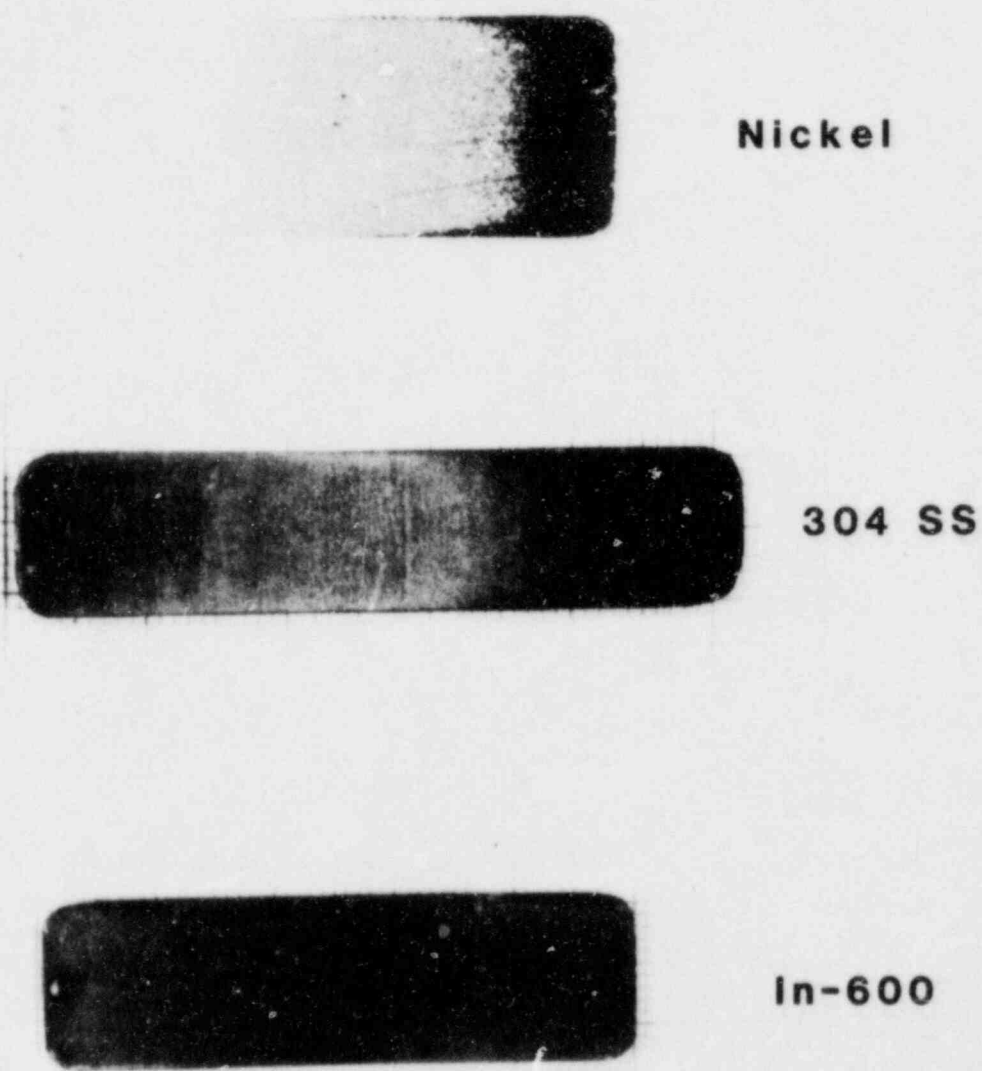


Figure 2. Appearance of Reacted Coupons Illustrating Typical Reaction Production Distributions

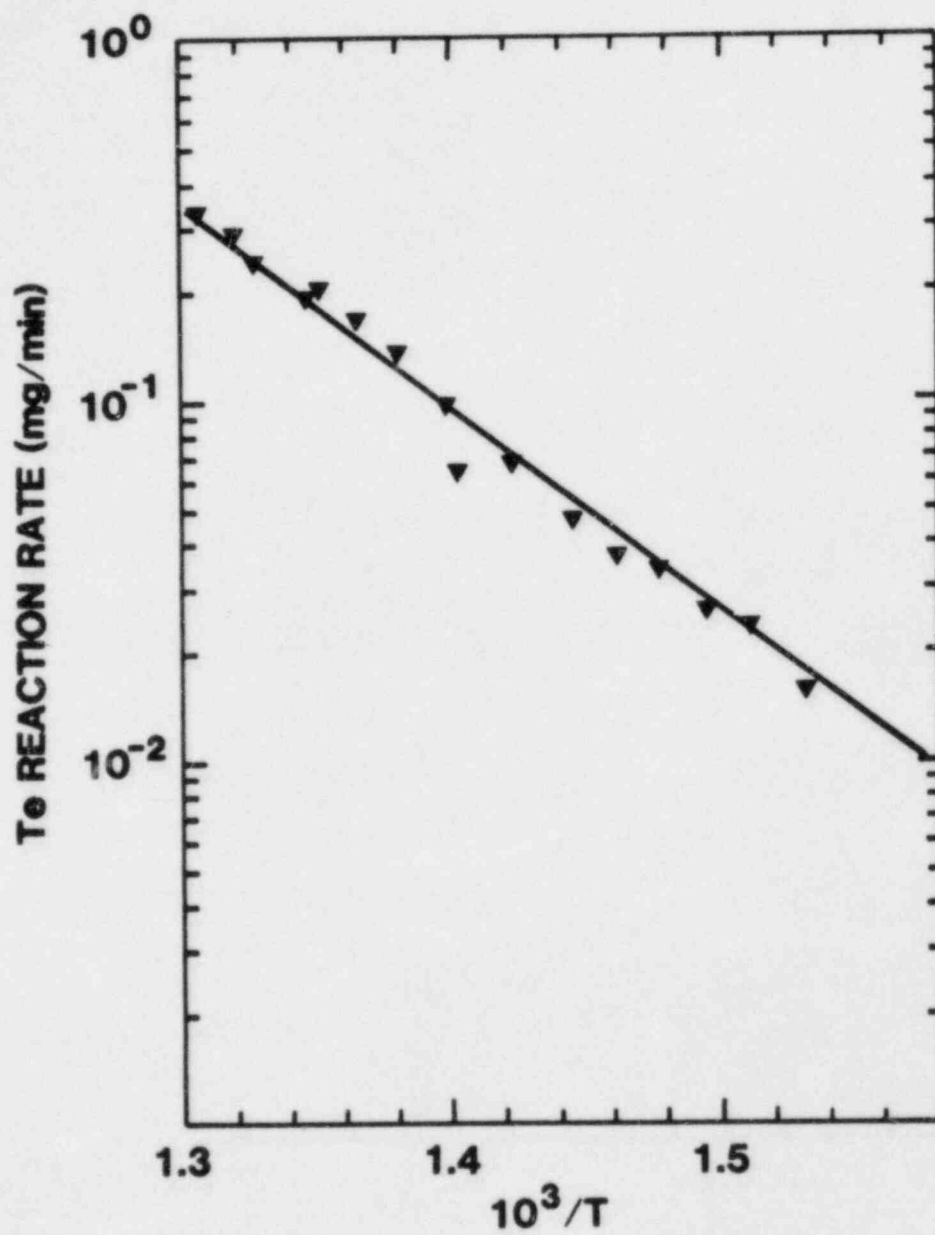


Figure 3. Measured Mass Gains Versus Reciprocal Tellurium Reservoir Temperature

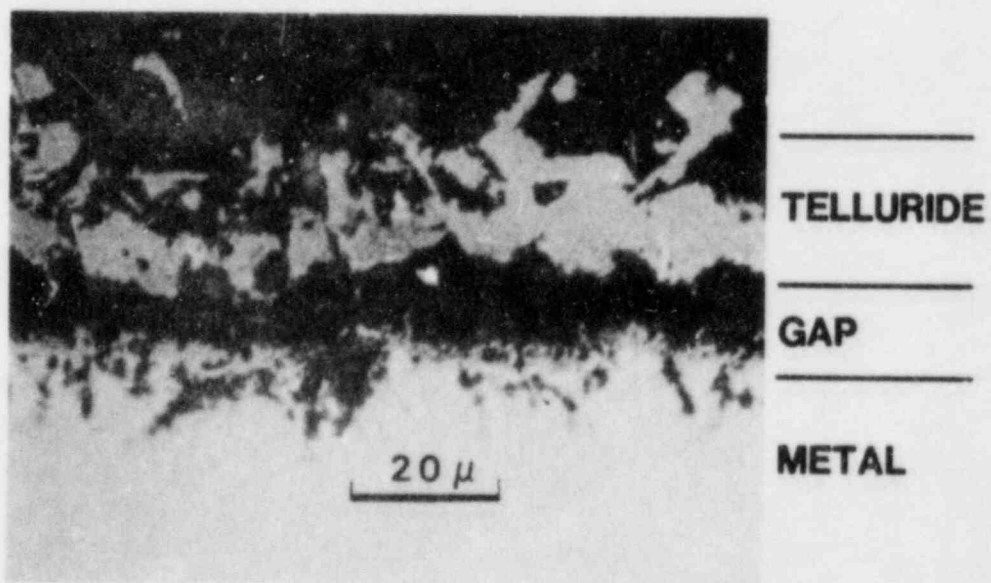
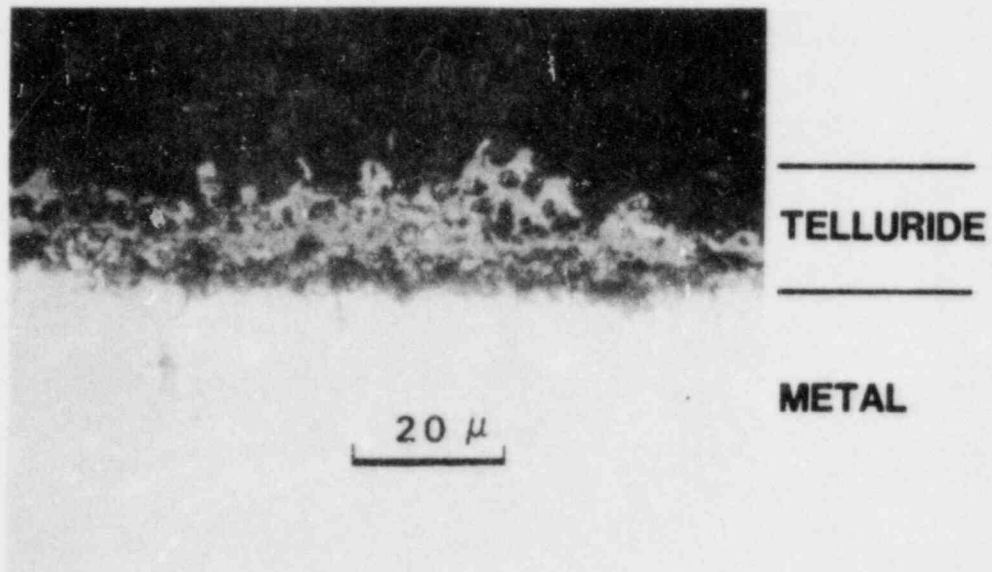


Figure 4. Cross Section of 304 Stainless Steel Alloy Exposed to Tellurium Vapor



Lobb and Robbins (Reference 8) reported that an amorphous iron and nickel telluride formed first on a 20 percent Cr/25 percent iron alloy. After 0.5 hour at high temperatures ( $T > 1023$  K), they observed the formation of a duplex layer consisting of an inner CrTe layer and an outer (Ni,Fe)Te layer. Continued annealing at high temperature caused the inner CrTe layer to grow and to consume the outer layer. This is consistent with the thermodynamic data (References 3, 4, 5) which shows that CrTe is more stable than any nickel or iron telluride.

At lower temperature (823 K and 923 K) short term anneals produced a single iron/nickel telluride layer containing little chromium. At 723 K, they report a nickel telluride is initially formed which at later times becomes a mixed iron/nickel telluride.

At 1123 K and after 10 hours, Anand and Pruthi reported that a duplex telluride layer had formed on 316 stainless steel (Reference 9). Again, the outer layer was rich in iron and nickel, while the inner layer was enriched in chromium.

We note that the experiments of References 8 and 9 were performed in sealed quartz tubes with a limited supply of tellurium. Given the speed of the reaction between tellurium and these alloys, it is apparent that for most of their experiments more time is spent annealing the reaction product than in actual reaction. The thermodynamic properties can thereby dominate. On the other hand, when there is a continual flux of tellurium to the metal surface as in the present experiments, kinetic factors will dominate and a mixed reaction product should result as we observe.

Several experiments were made to investigate the reaction of tellurium vapor with silver or Zircaloy-2. These data are also listed in Table B-I. Silver is a component of many control rods and may be present as bulk metal or as aerosol. Our single experiment with a silver coupon indicates rapid and complete reaction with tellurium. Figure 5 shows the appearance of the coupon after exposure to  $Te_2$  vapor. In contrast to 304 stainless steel and Inconel 600, where the reaction product coated the metal surfaces, the resultant silver telluride grew as fine needles emanating from the surface. Typical dimensions are 2 mm length by 0.1 mm to 0.2 mm diameter. The growth mechanism is not known and such needles may not be obtained in reactor accident conditions.

Zircaloy-2 is widely used to encase the  $UO_2$  nuclear reactor fuel. It is susceptible to oxidation by high temperature steam ( $T \geq 900$  K). However, the inner surface facing the  $UO_2$  may experience an interaction with fission product tellurium.



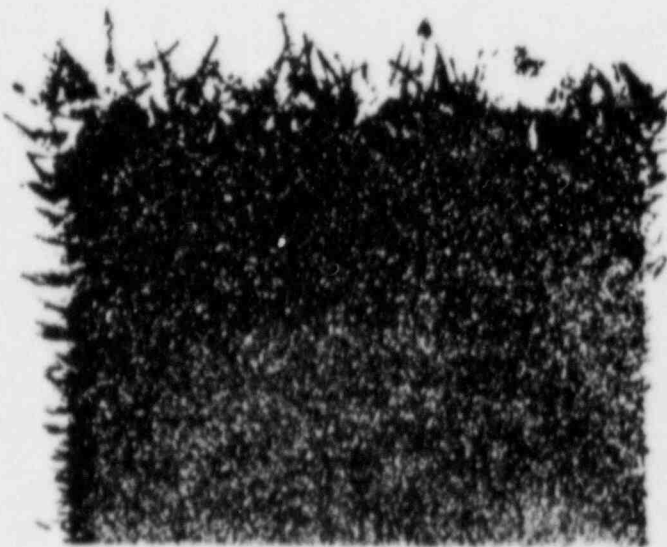
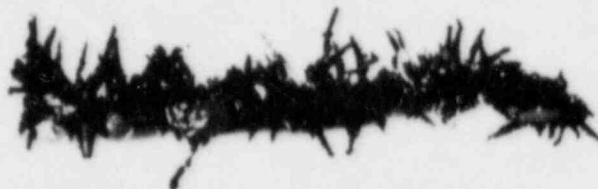


Figure 5. Appearance of Silver Coupon After Exposure to Tellurium Vapor

We studied the reaction between tellurium vapor and Zircaloy-2 at temperatures between 773 K and 1073 K. No reaction was observed when specimens were first exposed to tellurium vapor at 773 K. When the same specimen was then heated to 1073 K, an initially fast reaction was observed which slowed with passing time. Lowering the specimen temperature in 100 K increments further reduced the rate of reaction until at 773 K the rate was again too slow to measure.

The measured decrease in reaction rate observed when temperature was decreased would indicate a high (>50 kcal/mole) activation energy for the rate controlling process which could be the diffusion of either zirconium or tellurium ions through the reaction product. However, this would not explain why no reaction was initially measured at 773 K since there would not have been a sufficient reaction product present to restrict the reaction.

We believe a plausible explanation is that residual oxygen-containing impurities in the argon carrier gas cause the formation of a thin oxide layer on the alloy surface and that this oxide layer impedes the tellurium reaction. This oxide layer would tend to disappear at higher temperatures as a result of enhanced oxygen diffusion into the bulk alloy, and thereby facilitate the tellurium reaction.

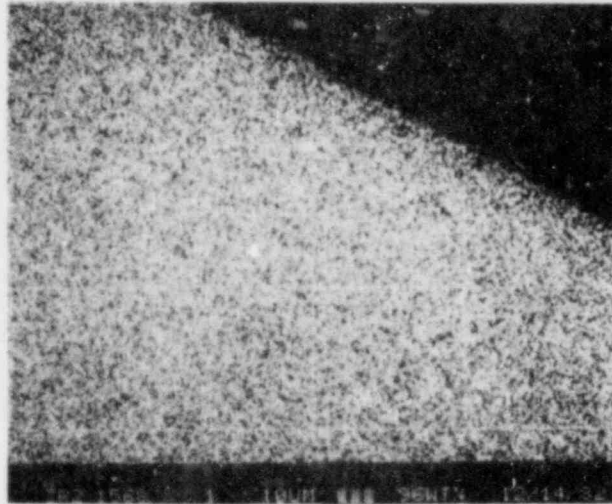
If a zirconium oxide layer does impede the reaction of tellurium, then it is quite likely that no interaction of tellurium and zirconium will be observed in the steam environment of a severe reactor accident.

X-ray diffraction methods have tentatively identified the high temperature reaction product as (ZrTe). There is some question as to its precise composition. Elliott (Reference 12) lists  $Zr_3Te_2$  as the phase in equilibrium with zirconium metal. A more recent phase diagram by Sodick, et al (Reference 13) puts this phase as  $Zr_6Te_5$ .

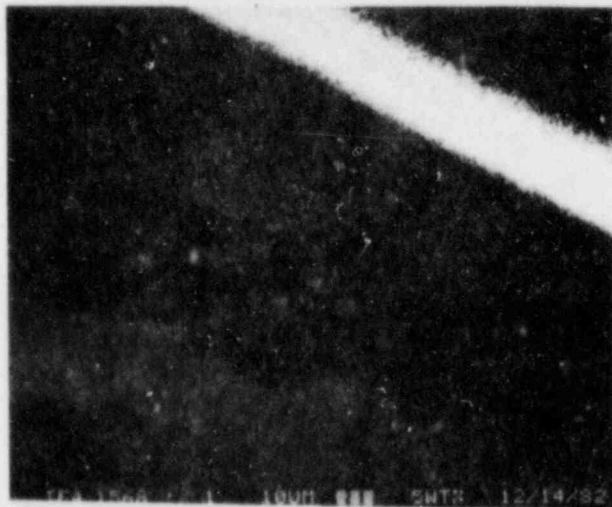
One sample coupon was sectioned and examined. Elemental distributions obtained with a scanning electron microscope (SEM) indicate that there is no diffusion of tellurium into Zircaloy-2 (Figure 6). Anand and Pruthi (Reference 9) reported that a duplex layer is formed when tellurium vapor reacts with Zircaloy-4. The present data do not indicate that any duplex layers are formed.

#### B. Reaction With Preoxidized Alloys

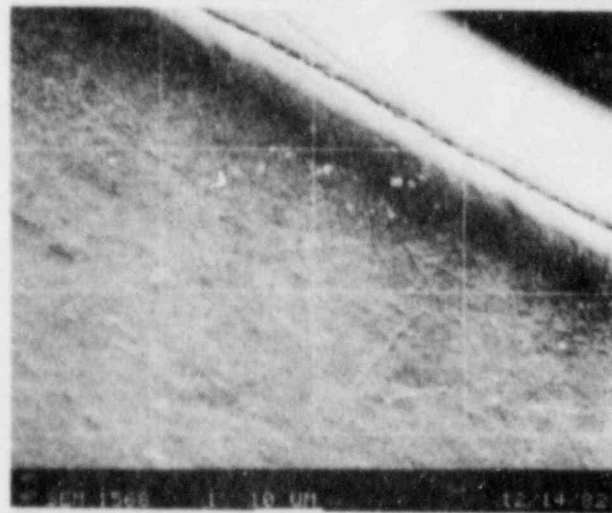
Gravimetric techniques, while very suitable for studying single processes, can be awkward to interpret when multiple processes--simultaneous oxidation and telluriding, for instance--are involved. Still, an assessment of the effect of oxidation is needed. We decided to preoxidize the alloys



Zr



Te



SEM

Figure 6. Elemental Distribution of a Cross Section of Zircaloy-2 Exposed to Tellurium Vapor

before exposing the alloys to tellurium vapors and to determine the effect of this oxide layer on reaction rate and reaction product. The chosen preoxidation process was the exposure of the alloy samples to an argon carrier gas which had been saturated with respect to water vapor ( $\sim 2.2$  KPa  $H_2O$  partial pressure, equivalent to 2.7 volume percent at our local conditions). The exposure time was 2 hours at 1373 K.

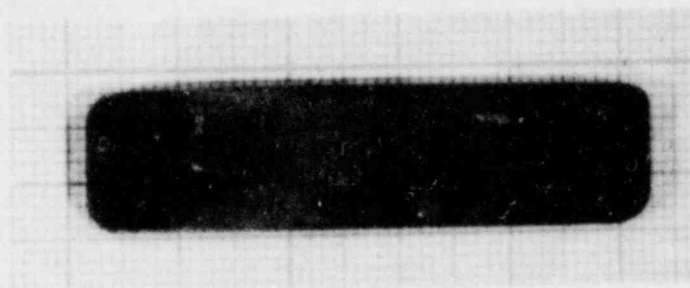
The oxide layer produced in 304 stainless steel was magnetite,  $Fe_3O_4$ , which contained only  $\sim 0.5$  weight percent each of nickel and chromium. The mass uptake was  $6 \times 10^{-3}$  gm  $O/cm^2$ . On Inconel 600, the resultant oxide was identified from its x-ray diffraction pattern as  $Cr_2O_3$ . The mass uptake was less than on the stainless steel, only  $2 \times 10^{-3}$  gm  $O/cm^2$ .

The experimental data for the exposure of these alloys to vapor are given in Table B-III. The results have some similarity to the unoxidized material:

- a) there was a linear rate of mass gain,
- b) this linear rate was proportional to the tellurium partial pressure,
- c) the linear rate did not change with sample temperature between 773 K and 1273 K,
- d) however, the reaction product was more widely distributed on the sample surfaces (see Figure 7),
- e) the composition of the reaction product varied along the length of the samples.

As with the unoxidized specimens, one deduced that here also substantially all the  $Te_2$  vapor had reacted with the oxidized material. The wider distribution pattern does indicate that the reaction of  $Te_2$  with oxidized metals, while fast, is slower than its reaction with unoxidized metal surfaces.

Not all the reaction products could be identified from the x-ray diffraction data. On the preoxidized 304 stainless steel, the leading surfaces, those which first "see" the tellurium-laden argon carrier gas, were found to contain  $FeTe_2$  as the reaction product. On the trailing surfaces, the reaction product was identified as  $Fe_{2.25}Te_2$ . No chromium telluride,  $CrTe$ , was detected in any x-ray diffraction patterns (detection limit  $\sim 3$  percent). The reaction product at intermediate distances (middle surfaces) could not be identified from their x-ray diffraction patterns. Two or more substances appear to be present.



**Inconel 600**



**304 Stainless Steel**

Figure 7. Appearance of Preoxidized Coupons After Exposure to Tellurium Vapor



The Fe+Te phase diagram (Reference 14) shows several compounds intermediate in composition to  $\text{Fe}_{2.25}\text{Te}_2$  and  $\text{FeTe}_2$ . These compounds are reported to be unstable at room temperature. The  $\beta$  phase  $\text{Fe}_5\text{Te}_6$  is said to be stable only between  $636^\circ\text{C}$  and  $809^\circ\text{C}$  (909 K and 1082 K), while the  $\delta'$ -phase ( $\text{Fe}_2\text{Te}_{3-x}$ ) is shown as stable only between  $519^\circ\text{C}$  and  $766^\circ\text{C}$  (792 K and 1039 K). It is not unreasonable to postulate that these compounds might be quenched without decomposition and to attribute the unidentified diffraction pattern(s) to these compounds.

The results for preoxidized Inconel 600 are quite analogous to the above. The reaction product at the leading surfaces is  $\text{NiTe}_2$  while at the trailing surfaces, the product is  $\text{Ni}_{2.86}\text{Te}_2$ . As with the stainless steel, there was no evidence for  $\text{CrTe}$  in the diffraction patterns. Likewise, the reaction product at intermediate distances could not be identified from the diffraction patterns.

The phase diagram of the Ni+Te system also shows intermediate tellurides (Reference 15). Some of these are stable to room temperature. We postulate that there is a decrease in the Te/Ni ratio of the reaction product along the specimen length and that the diffraction patterns at intermediate distance can be attributed to these intermediate compounds. If so, is there a logical basis for such a decrease of Te/Ni and Te/Fe ratios in their respective alloys? We believe that there is.

The particular reaction product which is formed must be related to the relative fluxes of tellurium and metal to the reaction zone. On unoxidized metal, the reaction is limited by the gaseous diffusion of  $\text{Te}_2$  vapor to the surface; the metal flux is not limited so that the telluride that is formed has the lowest possible Te/M ratio. On oxidized metal, the flux of the metal can be limited by the oxide layer if the telluride forms on the oxide/gas interface. This is the case. When a preoxidized and telluride specimen is sectioned and the elemental distributions measured with the microprobe, tellurium is found only on the exterior oxide surface (Figure 8). The metal flux to the reaction zone is the diffusive flux of metal ions through the oxide which is controlled by the oxide thickness.

These x-ray diffraction data are interpreted to mean that at the leading surfaces the vapor  $\text{Te}_2$  flux to the surface is larger than the flux of Fe or Ni ions through the respective oxide layers, thus forming  $\text{FeTe}_2$  (on 304 stainless steel) or  $\text{NiTe}_2$  (on Inconel 600). These reactions, of course, decrease the concentration of  $\text{Te}_2$  in the gas phase so that surfaces experience a reduced  $\text{Te}_2$  flux. The metal ion flux, however, remains unchanged with the result that the ratio of the tellurium flux to the metal ion flux decreases. The reaction

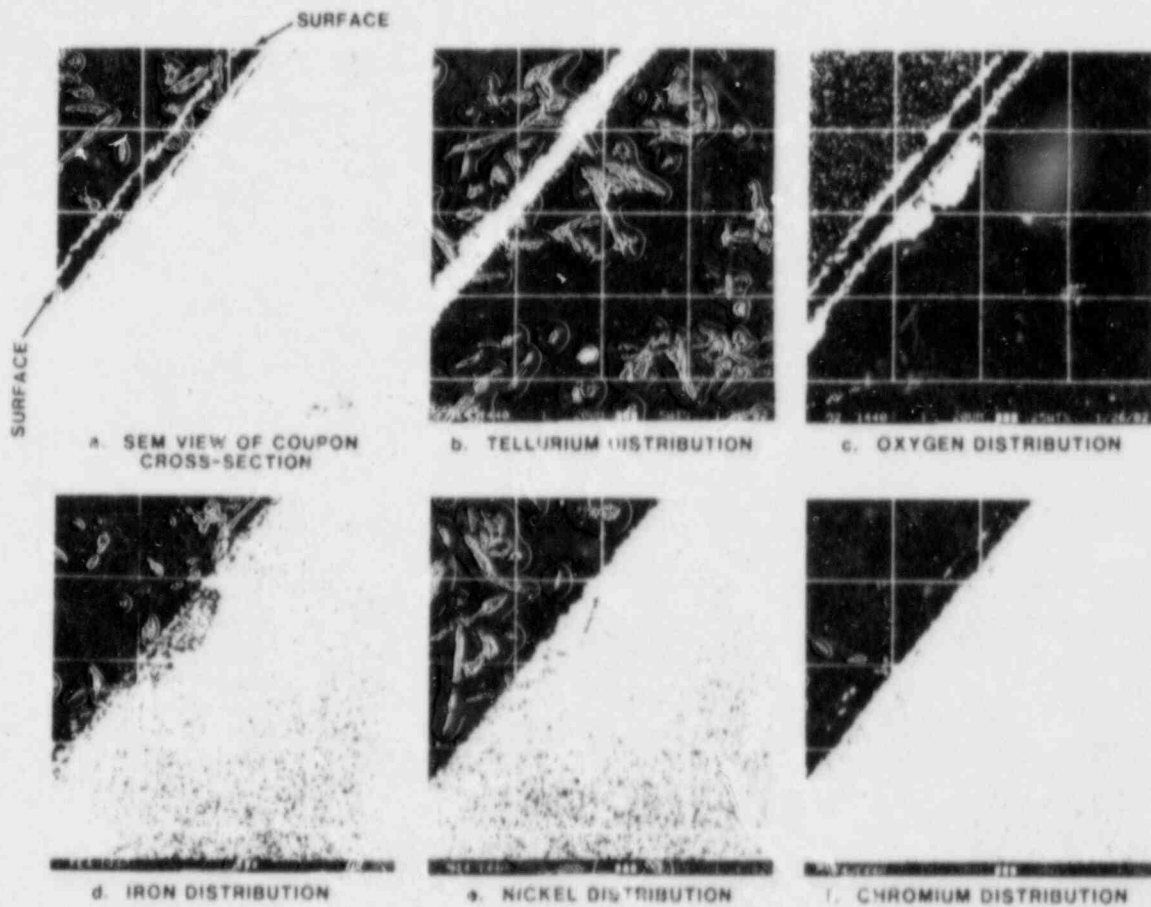


Figure 8. Elemental Distribution of a Cross Section of Preoxidized 304 Stainless Steel After Exposure to Tellurium Vapor



product composition reflects this new ratio. At the trailing surfaces, the  $\text{Te}_2$  flux is less than the metal flux and the product with lowest  $\text{Te}/\text{M}$  ratio is formed.

### C. Surface Reaction Kinetics--Application of FLATDEP Model

Computer modeling of fission product reactions generally use a simplistic approach. The TRAP-Melt code (Reference 13) uses the concept of "deposition velocity" to model the reaction of vapor species with solid surfaces. Here the net flux of a vapor species to a surface is taken to be proportional to the vapor phase concentration of that species (Equation (I)).

$$J_s = - \frac{1}{A} \frac{dm}{dt} = -v_d C_s \quad (\text{I})$$

If the vapor phase concentration,  $C_s$ , is measured in ( $\text{gm}/\text{cm}^3$ ) and the net flux to the surface,  $J_s$ , is measured in ( $\text{gm}/\text{cm}^2 \text{ sec}$ ), then the proportionality constant,  $v_d$ , has the dimension ( $\text{cm}/\text{sec}$ )--hence, the name deposition velocity.

Gravimetric measurements can, in most cases, result in a quantitative determination of the deposition velocity. If the amount of a species absorbed or deposited on a surface is small relative to the quantity of that species present in the vapor phase so that the vapor concentration is not significantly altered, then Equation (I) can be used directly. Even if there is a significant reduction in vapor concentration quantitative values for  $v_d$  can be obtained by using Equation (II), essentially an integrated form of Equation (I):

$$v_d = \frac{F}{A} \ln \frac{C_0}{C} \quad (\text{II})$$

In this equation,  $F$  is the volume flow rate of carrier gas;  $A$  is the area of sample surface; while  $C_0$ ,  $C$  are the initial and final vapor phase concentrations of the reacting or depositing species. This equation loses sensitivity whenever  $C < 0.1 C_0$  unless very precise measurements of concentration can be made. This is definitely not the case for our tellurium absorption experiments.

The deposition velocity  $v_d$  as used in such expressions is an overall rate constant combining the effects of both mass transport and surface reactions. In order to estimate surface reaction rates at the telluriding surface from the experimental data, the FLATDEP code has been developed at Sandia. It is briefly described in Appendix A. The code has been used to estimate the actual surface reaction rate of tellurium with the metal surfaces. The rate constant values deduced thereby refer to that surface reaction process and must be coupled with mass transport calculations in order to determine the tellurium reaction flux at some general surface.

The modeling of the flat surface with a cylinder presented great difficulties, thus, the code geometry was altered to a more tractable form, that of a flat surface with a rectilinear table. Deposition patterns were calculated assuming various values for the surface reaction rate constant  $k_f$ .

These calculations indicated that in order to obtain >95 percent deposition (absorption) of tellurium, a value of  $k_f > 10^{-3}$  m/sec was required. These calculations also indicated that nearly identical deposition patterns were obtained whenever  $k_f \geq 10^{-1}$  m/sec. In these latter cases, the deposition was limited by the arriving flux of tellurium vapor and not by surface reactions.

As can be seen in Figure 9, for  $10^{-3} < kc_d < 10^{-1}$  m/s, estimates of  $k_f$  can be made from the length of the deposition region. For unoxidized specimens,  $k_f$  is estimated to be at least  $10^{-1}$  m/sec. (The deposition pattern is particularly evident for  $Te_2$  on Ni, Figure 2a). Larger values can not be excluded, however. For oxidized specimens,  $k_f$  is estimated to be  $10^{-2}$  m/sec. The x-ray diffraction data indicates that some telluride is formed even at the trailing surface while balance data indicate that >95 percent of tellurium vapor has reacted or deposited on the preoxidized surface.

#### D. Desorption Measurements

The original goal of this section has been to measure the desorption rates of tellurium from the various telluride reaction products. To use a microbalance technique would require a uniform composition over the surface of any specimens. However, as was seen in the previous sections, a uniform product definitely was not formed in the absorption experiments. Efforts were made to produce the desired uniform reaction product using the techniques of references (8) and (9)--ie, heating metal and tellurium in sealed evacuated glass containers. We were not successful in these efforts; visually nonuniform coatings were obtained.

In the course of these attempts, we noted that solid solutions of tellurium in nickel and 304 stainless steel could be made. When heated at 1273 K for 68 hours, bright specimens were obtained whenever the mass ratio (Te:metal) was 0.004 gm/gm or less, while dull surfaces resulted at greater ratios. The solubility of tellurium in nickel and stainless steel is thus about 0.2 atom percent at 1273 K.

Desorption measurements were made on those specimens containing 0.004 gm Te/gm metal. We assumed that there was initially a uniform concentration of tellurium in the metal. In this case, one would expect a constant maximum desorption rate of tellurium until its surface concentration, which is being replenished in part by diffusion of tellurium from the interior, decreased to some critical value. The duration of

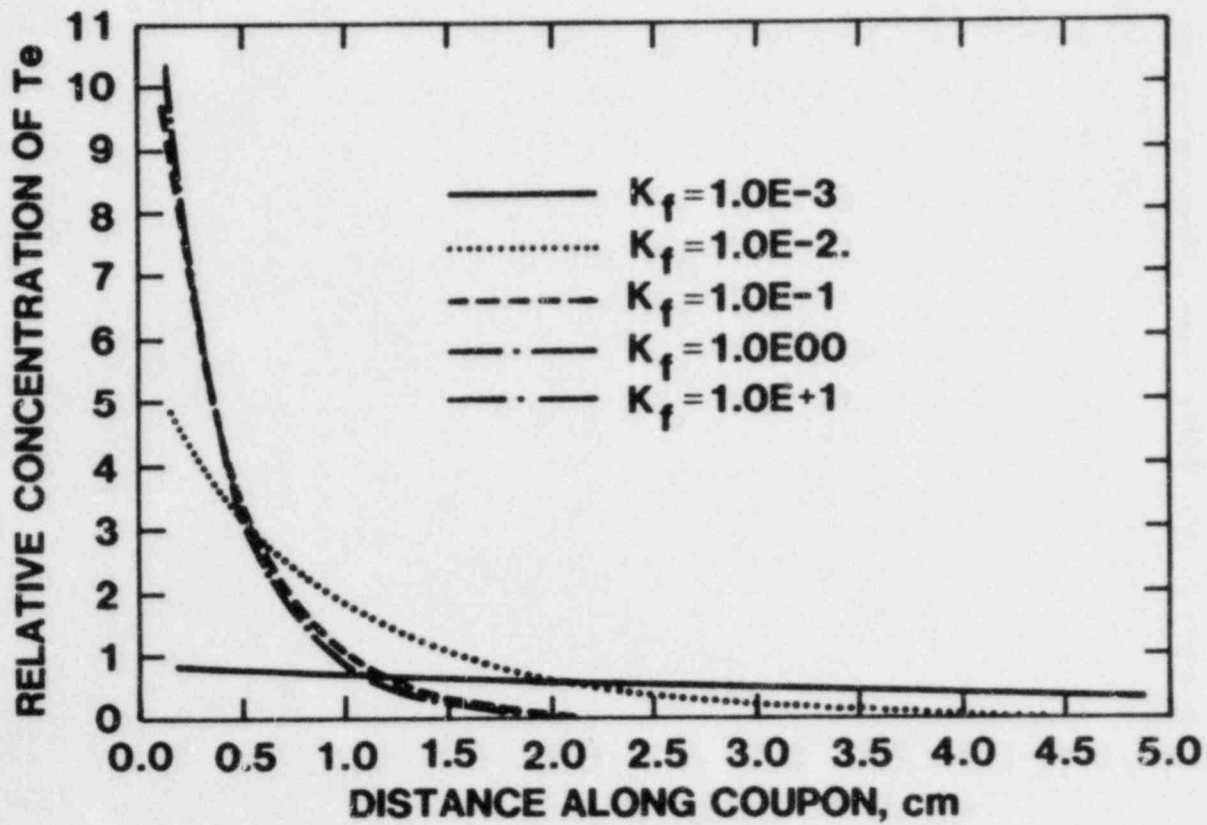


Figure 9. A Plot of Calculated Tellurium Deposition for Various Assumed Values of the Surface Reaction Rate Constant

this maximum desorption depends on sample temperature and is lengthened at higher temperatures because the rates of solid state diffusion of tellurium increase as temperature is raised.

Carrier gas flowed past the specimens at rates between 0.025 and 0.10 liter/minute but largely at 0.05 liter/minute. With the nickel specimens the carrier gas was argon plus 1 percent hydrogen. The latter was added to prevent any possible oxidation of nickel by impurities which might be present in the gas stream. The effect of water vapor on the desorption process was investigated when the carrier gas was bubbled through liquid water on its way to the balance apparatus.

With 304 stainless steel specimen, the presence of hydrogen would not prevent oxidation of the chromium component by water vapor or other oxygen impurities. Hence, hydrogen was not added to the argon. Instead, the argon was further purified by passage through hot zirconium metal turnings (at 1173 K) immediately before entering the balance apparatus.

The desorption rate of tellurium was measured over the temperature range of 1073 K to 1173 K (800°C to 900°C). We accepted for analysis only those rates which were constant with time. (Nonlinear rates were attributed to limitations by solid state diffusion.) These data are plotted to Figure 10 for the tellurium-in-nickel solid solution and in Figure 11 for the tellurium-in-304 stainless steel solid solution. These data were fitted to Arrhenius-type equations. For the nickel solid-solution, the resultant equation is

$$\log_{10}(k) = (5.36 \pm 0.75) - \frac{(10405 \pm 881)}{T(K)}$$

where  $k$  is expressed in  $\text{mg}/\text{cm}^2\text{-min}$ , and  $T$  is expressed in  $K$ . The corresponding equation for the stainless steel solid-solution is

$$\log_{10}(k) = (5.21 \pm 1.40) - \frac{(10370 \pm 1640)}{T(K)}$$

These conclusions were reached:

- a) Because these rates are linear (independent of time) diffusion of tellurium from the interior of these solid solutions was not a limiting rate process. Deviations from linearity were observed when approximately one-half of the original tellurium content had been removed.

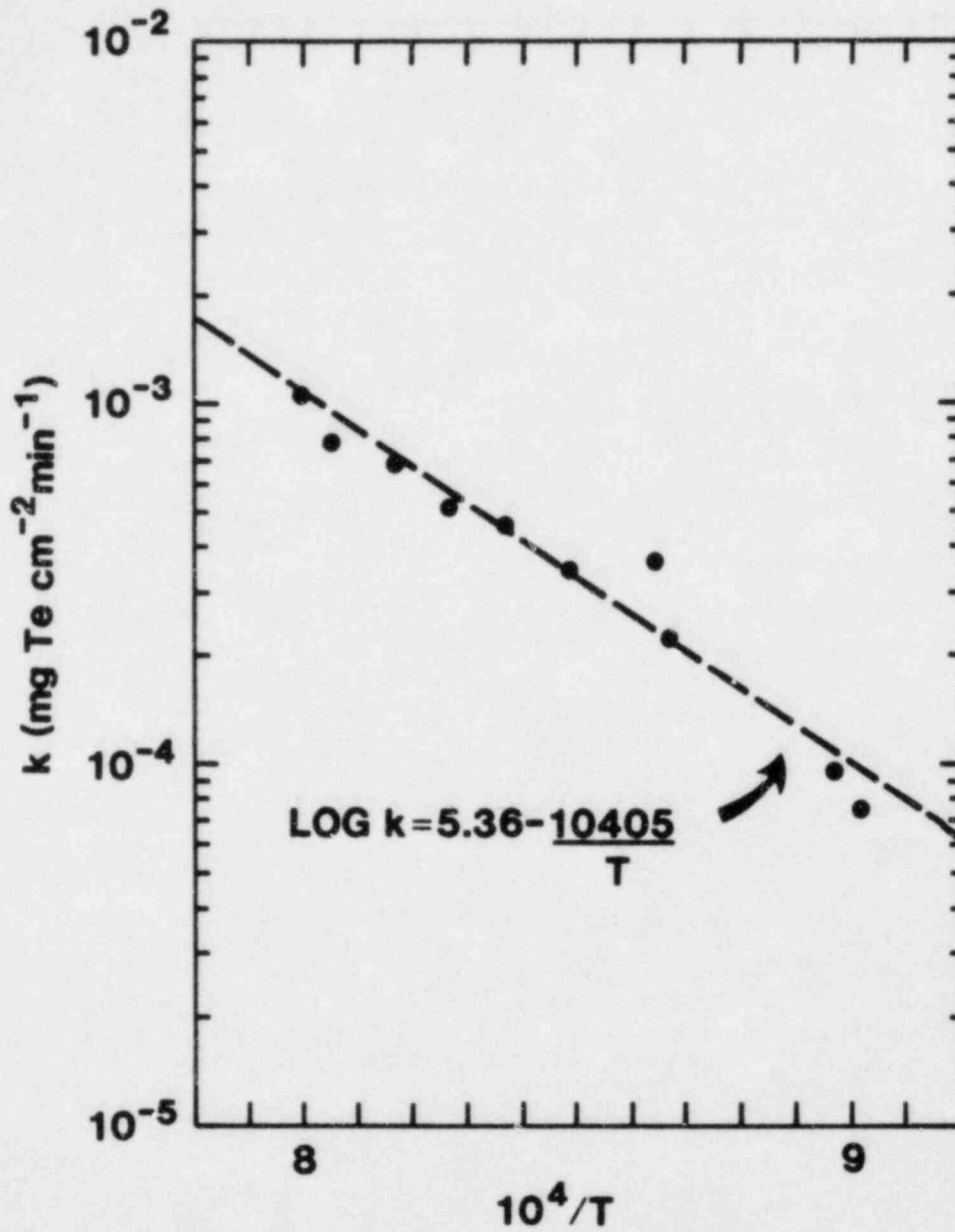


Figure 10. Desorption Rates of Tellurium for Tellurium-in-Nickel Solid Solution



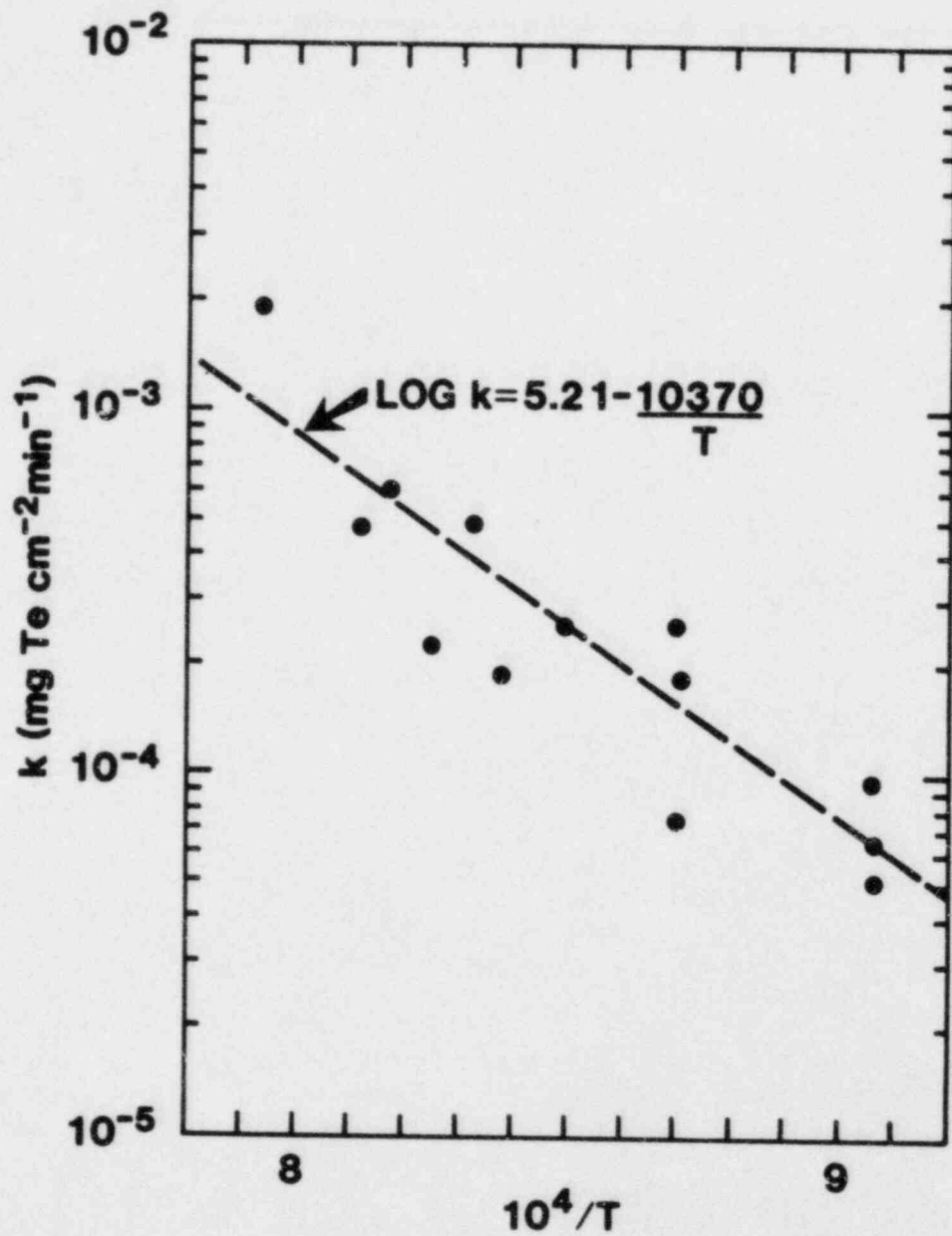


Figure 11. Desorption Rates of Tellurium for Tellurium-in-304 Stainless Steel Solid Solution

- b) Over the restricted flow range used in these experiments, the desorption of tellurium was unaffected by the magnitude of the gas flow, suggesting that the rate-limiting step is indeed the desorption of tellurium from the surface, and not the establishing of local equilibrium conditions in the adjacent gas phase.
- c) The presence of water vapor did not inhibit or otherwise affect the desorption of tellurium from the nickel solid-solutions. It is recognized, however, that oxide formation may serve as a barrier to tellurium desorption.

#### IV. Summary

An original purpose of the Sandia Fission Product chemistry program was to delineate the significant reactions occurring in a severe reactor accident environment in which fission product elements participate. As a result, the tests described herein have an inherent scoping nature. Nevertheless, the generated data have sufficient quality that a more detailed insight into the tellurium reactions is possible than might have been originally anticipated.

These tests demonstrate that tellurium vapors are very reactive species and that there is good potential for the retention of fission product tellurium within the primary system of a light water reactor. Specifically, the structural alloys--304 stainless steel and Inconel 600--can be efficient sinks for tellurium. Moderate oxide coatings do not appreciably impair the reaction of tellurium with these alloys. The primary reaction products have been identified:  $Ni_{2.86}Te_2$  on Inconel 600 and  $Fe_{2.25}Te_2$  on 304 stainless steel. The compounds  $NiTe_2$  and  $FeTe_2$  are also found when there is an oxide layer present.

Deposition profiles have been calculated using a computer code which models both the surface tellurium reaction and the gas phase transport. These profiles were compared to the experimental observations and order of magnitude estimates of surface reaction rate constants were deduced. These values range between 1 and 10 cm/sec for the unoxidized structural alloys and 0.1 to 1 cm/sec for preoxidized alloys. These values are much larger than we expected.

Silver, a major component of some control rods and a probable aerosol constituent, has been shown to react rapidly with tellurium vapor. The surface reaction rate constant is estimated to be 1 cm/sec. As a consequence, fission product tellurium may be transported out of the primary system whenever silver aerosols are present.



There is a reaction of tellurium vapor with zircaloy-2, used as a cladding material for nuclear fuel rods. Our data indicates that the reaction is strongly temperature dependent and that there is no incorporation of tellurium into a solid solution with zirconium.

Lastly, the desorption of tellurium from solid solution with 304 stainless steel and with nickel, the basic element of Inconel 600 alloy, have been measured.

These data, while illustrating the reactivity of tellurium with reactor materials, cannot be applied indiscriminately to the severe accident environment. An important vapor constituent, steam, was not present. Our future work will explore the effect of steam and the resultant simultaneous oxidation of these alloys on the tellurium reactions.

## V. References

1. "Technical Bases for Estimating Fission Product Behavior During LWR Accidents, Chapter 4-Fission Product Release From Fuel," NUREG-0772, June 1981.
2. *ibid*, "Chapter 5-Chemistry of Cesium and Iodine," NUREG-0772, June 1981.
3. M. Ettenberg, K. L. Komarek, and E. Miller, "Thermodynamic Properties of Nickel-Tellurium Alloys," *J. Solid State Chem.* 1, 583 (1970).
4. Isper and K. L. Komarek, "Thermodynamic Properties of Iron-Tellurium Alloys," *Monat. Chem.*, 105, 1344 (1974).
5. H. Isper, K. O. Klepp, and K. L. Komarek, "Thermodynamic Properties of Chromium--Tellurium Alloys," *Monat. Chem.* 111, 761 (1980).
6. J. E. Antill and R. F. S. Carney, "Attack of Stainless Steel by Tellurium/Oxygen/Caesium Corrodents at 350°C to 678°C," *J. Nucl. Mat.*, 88, 212 (1980).
7. J. E. Antill and J. B. Warburton, "Influences of Tellurium on Caesium-Enhanced Corrosion of Stainless Steel," *J. Nucl. Mat.* 71, 134 (1977).
8. R. C. Lobb and I. H. Robbins, "A Study of the 20 Percent Cr/25 Percent Ni/Nb Stabilized Stainless Steel-Tellurium Reaction," *J. Nuc. Mat.* 63, 50 (1976).
9. M. S. Anand and D. D. Pruthi, "Surface Reactions of Tellurium on Steel and Zircaloy 4" India, A.E.C., Bkabh At. Res. Cent. Report. B.A.R.C.-1009 (1979).
10. Handbook of Chemistry and Physics, 62nd Edition, 1981-1982 CRC Press, Boca Raton, FA.
11. Joint Committee of Powder Diffraction Standards, Temple University, Philadelphia, PA.
12. R. P. Elliott, "Constitution of Binary Alloys, First Supplement," McGraw-Hill Book Co., New York (1965).
13. H. Sodeck, H. Mikler, and K. L. Komarek, "Transition Metal-Chalcogen Systems VI: The Zirconium-Tellurium Phase Diagram," *Monot. Chem.*, 110, 1 (1979).
14. H. Isper, K. L. Komarek, and H. Mikler, "Transition Metal-Chalcogen Systems, V: The Iron-Tellurium Phase Diagram," *Monat. Chem.*, 105, 1322 (1974).
15. K. O. Klepp and K. L. Komarek, "Ubergangsmetall-Chalkogensysteme, 3. Mit.: Gas System Nicel-Tellur," *Mont. Chem.*, 103, 934 (1972).

## APPENDIX A -- Estimation of Surface Reaction Rate of Tellurium Vapor From Observed Deposition Profiles

This appendix describes the calculational procedure used to interpret the results of the experiments in terms of a rate expression for the reaction of tellurium vapor at the metal surface. As a first approximation, it has been assumed that this reaction is first order with respect to the tellurium concentration in the adjacent gas phase, and that no desorption occurs once the tellurium has been deposited. The first order rate constant for a heterogenous reaction at a surface has the dimensions  $LT^{-1}$ . It should not be confused with the deposition velocity which has the same dimensions but is generally used as a net removal rate constant including the effects of mass transfer through the gas. The work described here permits the effects of mass transfer and surface chemistry to be separated, an essential prerequisite for obtaining a description of the actual surface reaction kinetics.

### Calculational Method

The geometry of the system used in these Sandia experiments--a flat, rectangular coupon placed along the direction of flow inside a cylindrical tube--gives rise to a complex laminar flow pattern of the gas around the coupon, and thus to a nonuniform pattern of tellurium deposition across its width. The system geometry, and typical results, are illustrated in Figure 1 of the main text. This system represents an extremely difficult problem for the evaluation of tellurium vapor transport to the coupon surface, and the first step in the calculational route is therefore to approximate this system and result by a representation more amenable to solution. A simple, one-dimensional representation was chosen and is described below. With this simplified geometry, the flow pattern of the argon carrier gas can be calculated analytically.

Once the carrier gas flow is known, the differential equations describing tellurium vapor transport along the flow direction and diffusion across it to the coupon surface can be set up. The asymmetric boundary conditions in this system (tellurium reacts only at the surface on one side of the flow channel) preclude a simple analytical solution, and the transport problem is therefore solved numerically.

Having developed a computer program to calculate the deposition profile resulting from a specified surface reaction rate constant, the value of that rate constant may be varied so as to obtain a best fit to the experimental result. The rate constant thus obtained is subject to three major uncertainties:

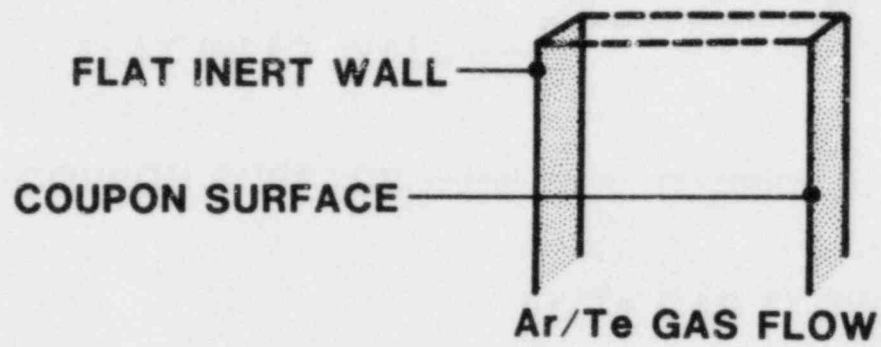
- i) How accurately does the model geometry approximate the exact solution of the differential equation system;
- ii) How well does the numerical solution approximate the exact solution of the differential equation system; and
- iii) Is the assumption of a first-order, irreversible surface reaction adequate?

The likely extent of these uncertainties may be estimated and minimized as follows:

- i) By varying the model parameters between the limits deducible from the real system--errors in modelling the flow system might result in a factor of 1.5 or 2 uncertainty in the calculated deposition profiles (which might correspond to a much wider range of deposition velocity values).
- ii) The calculational mesh into which the system is split can be varied and the effect on the solution investigated. In particular, the mesh spacing can be reduced to the point beyond which further reduction has no effect on the solution. In practice, this highly desirable "exact" solution is often prohibitively costly, since the number of nodes, and hence of variables required to achieve it, is so large. It is usually desirable, therefore, to sacrifice some small percentage of accuracy in the interests of economy.
- iii) The validity of the surface chemistry model may be gauged from the success achieved in fitting the experimental results. Clearly a good match suggests that the model may be adequate, while if it proves impossible to adjust the parameters so as to obtain a good match, the model is in need of modification or refinement. The strength of the conclusions which may be drawn about the surface phenomena in this way depends critically on how well the other system processes have been modelled.

## 1. Geometrical Representation

The rather uniform "front" of deposited tellurium around the center of the coupons (Figure 2 of main text) suggests that, for this part of the coupon at least, it may be reasonable to assume that the system is equivalent to a flat coupon separated from a flat alumina wall parallel to it by a gas stream within which there are no velocity gradients across the width of the coupon. The system modelled, and a comparison of its cross-section and that of the actual system is illustrated in Figure A-1.



**CROSS-SECTIONS**

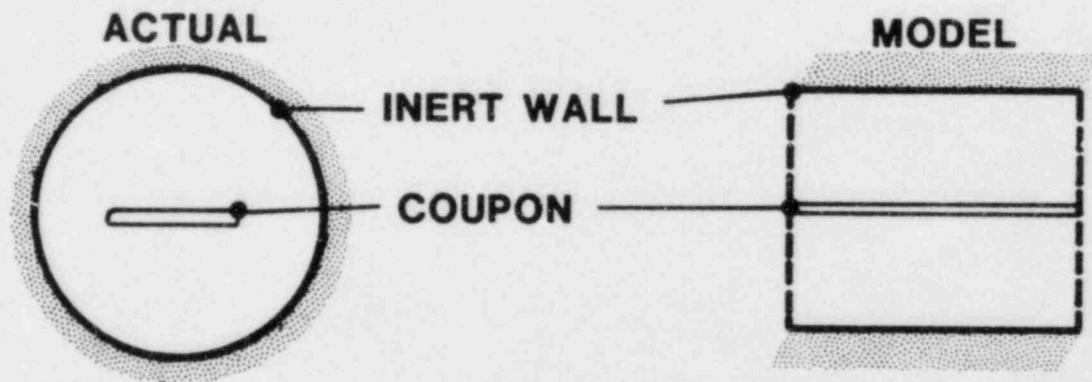


Figure A-1. The Experimental System--as Modelled



Although the system is one-dimensional, it is assigned a "width" such that its volume equals exactly one half that of the actual system. The argon gas flow rate is set at half that of the experiment (50 cm/minute at 293 K and 630 torr). The only parameter whose value is in doubt is the mean distance to be assumed to separate the coupon and the alumina wall. This could be taken as anything from the mean half-tube height (viewed in cross-section in Figure A-1) across the whole of the tube diameter, to that across the coupon width or even the radius of the tube itself. Unless otherwise stated, results in this note are presented for a separation which is equal to the mean taken over the coupon width.

## 2. Flow Between Parallel Plats

Ignoring entrance effects, the linear gas velocity as a function of distance from the mid-plane between a flat coupon and a flat wall may be derived in a manner exactly analogous to that used to derive the well-known Poiseuille formula for cylindrical geometry. A simple Reynolds number estimate demonstrates that the flow is laminar rather than turbulent:

$$Re = Dv\rho$$

where  $Re$  = Reynolds no.,  
 $D$  = equivalent hydraulic diameter,  
 $v$  = linear fluid velocity,  
 $\rho$  = fluid density, and  
 $\mu$  = fluid viscosity.

For argon gas at a temperature of 773 K, in this system, these properties have the following values:

$$\begin{aligned} D &= 0.017 \text{ m} \\ v &= 0.007 \text{ ms}^{-1} \\ \rho &= 0.523 \text{ kgm}^{-3} \text{ (ideal gas)} \\ \mu &= 4.5\text{E-}5 \text{ kgm}^{-1}\text{s}^{-1}, \end{aligned}$$

so that  $Re$  has a value of about 1.4--clearly well below the threshold of a few hundred around which laminar flow starts to break down. Note also that for so small a Reynolds number, the entrance length for the system (the length required for the flow to become fully developed) is on the order of a millimeter. Thus the neglect of entrance effects should not lead to significant error.

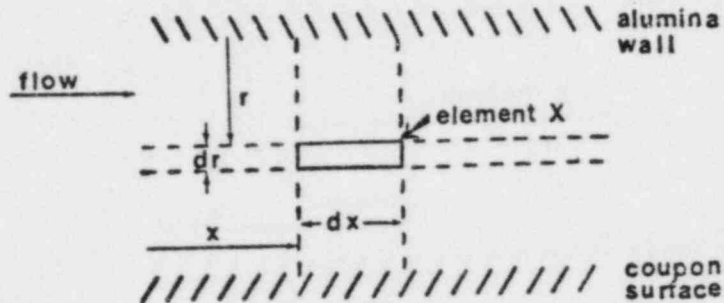
An expression for the flow calculation has been presented elsewhere (Reference A-2); the results is the linear flow rate at  $r$  in terms of the total volume flow rate  $V$

$$v(r) = \frac{3V (R^2 - r^2)}{4 R^3}$$



### 3. Differential Equations for Te Transport

Consider a small element X of gas of length  $\delta x$ , width  $w$  and thickness  $\delta r$ , located at a distance  $x$  downstream of the inlet and a distance  $r$  from the alumina wall, as shown in the diagram below:



Let  $c(r,x)$  be the concentration, and  $q(r,x,\delta r,\delta x)$  the total quantity of tellurium ( $g - \text{mol}/\text{m}^3$  &  $g - \text{mol}$  respectively) in element X.

The derivative of  $q$  (and thus of  $c$ ) has two components, one being the net flux  $J[x]$  of tellurium carried into X by the gas stream; the other being the net diffusional flux  $J[r]$  into X in the  $r$  direction.  $J[x]$  is given by

$$J[x] = v(r) w \delta r (c(r,x) - c(x+\delta x)) \quad (1)$$

$$= -v(r) w \frac{\partial c}{\partial x} \delta r \delta x$$

where angle brackets are used to denote partial derivatives and  $v(r)$  is obtained from Equation (1) above, with the value of  $r$  used in Equation (1) given by  $R-r$  for  $0 < r \leq R$  or  $r-R$  for  $R < r < 2R$ . From Fick's first law, the analogous expression for  $J[r]$  is:

$$J[r] = (-D w \delta x \frac{\partial c}{\partial r} (r,x)$$

$$(-D w \delta x \frac{\partial c}{\partial r} (r + \delta r, x)$$

$$= D w \delta x \langle \partial^2 c / \partial r^2 \rangle$$

where  $\partial^2 c / \partial r^2$  is the second derivative of  $c$  with respect to  $r$ , and  $D$  is the diffusion coefficient of  $\text{Te}_2$  vapor in argon. A value for  $D$  was estimated using the Wilke-Lee modification of the Hirschfelder-Bird-Spotz method (Reference A-1).

The derivative of  $q$  is obtained simply by summing  $J[r]$  and  $J[x]$ , so that since  $c = q/(w,dr,dx)$ , we have the following expression for the derivative of concentration:

$$c' = D \partial^2 C / \partial r^2 - V(r) \partial C / \partial x \quad (2)$$

Boundary conditions are given by:

$$\frac{\partial C}{\partial r} (0, x) = 0 \quad (3)$$

for all  $x$  at the alumina surface and

$$D \frac{\partial C}{\partial r} (2R, x) = k_f C(2R, x) \quad (4)$$

for all  $x$  at the coupon surface.

#### 4. Solution

For a simple system such as this one, it would be normal to use a Laplace transform method to obtain an exact, analytical solution to Equation (2) subject to conditions Equation (3) and (4). However, the form of the boundary conditions for this system, in particular their lack of symmetry around the  $r=R$  plane, renders this rather difficult. Equation (2) has accordingly been adapted for numerical solution, as described in Reference A-2.

#### 5. The FLATDEP Program

The computer program FLATDEP has been written at Sandia to solve the set of coupled ordinary differential equations resulting from discretization of the partial differential equation developed above with the aid of the library subroutine DDEBDF (Reference A-3). The program reads in details of the system such as geometry and gas flow rate, tellurium properties such as diffusion coefficient and deposition velocity, and an array of times at which output is required, and provides output giving the tellurium vapor pressure profile at various distances from the coupon surface as well as the profile of deposited tellurium along the coupon. The program at present includes the following features:

- i) A modular format, using separate subroutines for calculating mesh spacings and flow velocities within elements of the flow, enables the program to be adapted readily to other geometries.
- ii) The 2-D arrays of variables and their derivatives are mapped onto 1-D arrays prior to solution of the ODEs in such a way that the workspace required for solution is minimized. This tactic, combined with the use of the DDEBDF routine, which takes advantage of the sparsity of the matrices used in the solution, enables solution to be accomplished efficiently even when the number of variables involved is very large (up to several 100s).

- iii) The program tests for a steady-state at the end of each time step by comparing the vapor pressure profile along the coupon with that at the previous step. If the profiles match, execution is halted after a further small time step has been taken in order to determine the fraction of fission product penetrating the system once the steady-state has been reached.
- iv) The mesh used is equispaced in the x direction; the radial mesh spacings may be set in a variety of ways so as to concentrate the elements in the region close to the coupon surface.

The program has been used to demonstrate the effect of surface reaction rate constant on the deposition profiles anticipated for the Sandia experiments, and to assess the effect of various system parameters on these calculated deposition profiles. The 773 K experiments have been used throughout as a demonstration case; with the experimental system used to date it is not possible to resolve surface kinetics accurately enough to obtain the rate constant as a function of temperature over the range covered in experiments.

The sensitivity of the results to mesh spacings and geometrical parameters has been described in Reference A-2. Figure 11 of the main text shows the effect of different surface reaction rate constants on the calculated deposition profile. A rate constant of  $10^{-3}$  m/s gives an almost uniform profile, with only about a factor of 2 difference between the surface concentration of tellurium at the coupon "inlet" and "exit." Increasing the rate constant by an order of magnitude produces a profile with much more of the tellurium deposited at the front end of the coupon; there is a more than 10 fold drop in surface concentration by the mid-point along the coupon length. A further increase of a factor of 10 in the rate constant makes this effect even more marked; a 10 fold drop in concentration now occurs over the first centimeter of the coupon surface. Further increase, though, has little effect on the calculated deposition profile; the curves for rate constants of 1 and 10 m/s are indistinguishable from one another and differ only slightly from that obtained with a value of 0.1 m/s. Clearly, deposition is in these latter cases being limited by mass transfer through the gas rather than by the rate of the surface reaction.

To give some idea of where the transition from reaction rate limited to mass transfer limited, deposition takes place, the ratio of the surface concentration of Te on the first quarter of coupon (0 to 1.25 cm) to that on the second quarter (1.25 to 2.5 cm) is plotted as a function of  $k_f$  in

Figure A-2. It should be noted that around the region of interest ( $k_f \sim 0.1$  m/s) the slope of the curve is becoming rather shallow. This implies that it is rather difficult to deduce a deposition velocity from empirical data on the ratio of surface concentrations at different parts of the coupon as the curve in Figure A-2 is subject to considerable uncertainty owing to the inaccuracies in both the model and the parameters input to it.

Figures A-3 to A-5 illustrate the calculated variation of Te vapor pressure along the length of the coupon for three different values of the surface rate constant. These most obvious features are the increasing negative slope with increasing  $k_f$ , the linearity of the individual curves, and the fact that they are mutually parallel. The closeness of the curves for the alumina wall and the mid-plane between wall and coupon indicates that concentration gradients across the flow are highest close to the coupon surface. This is born out by the corresponding "radial" vapor pressure profiles plotted in Figures A-6 through A-8, which show, as would be expected, steeper gradients close to the coupon surface for the high surface reaction rate constants.

The effect of uncertainties in the input parameters to the model is illustrated in Figures A-9 and A-10, which respectively show the effects of a change of a factor of 2 in the estimated diffusion coefficient for the Te vapor in argon and a change of 20 percent in the assumed value for the separation between the coupon and the wall of the alumina tube. Both figures take the case of mass transfer-limited deposition, which should maximize the impact of parameter changes and more clearly demonstrate their effects. The diffusion coefficient seems to have a very large impact, whereas that of the changes in "SEP" is relatively small.

Finally, Figure A-11 illustrates the effect anticipated for a 4-fold increase in flow rate of the carrier gas. This demonstrates that increasing the flow rate alone does not lead to a separation of the curves obtained for higher surface reaction rates, suggesting that repeated experiments with high flow rates would not of themselves be sufficient to resolve the observed reaction rates to a higher degree of accuracy. If anything, increasing the flow rate will only make shallower the slope of curves of the type shown in Figure A-2, thereby making  $k_f$  values harder to resolve.

## 6. Conclusions

1. By inspection of Figures 1 and 11 of the main text, it may be deduced that the surface reaction rate constants for tellurium vapor on the coupon illustrated is certainly greater than 1 cm/s, and probably greater than 10 cm/s. Uncertainty in the parameters used in the calculations and in the modeling of

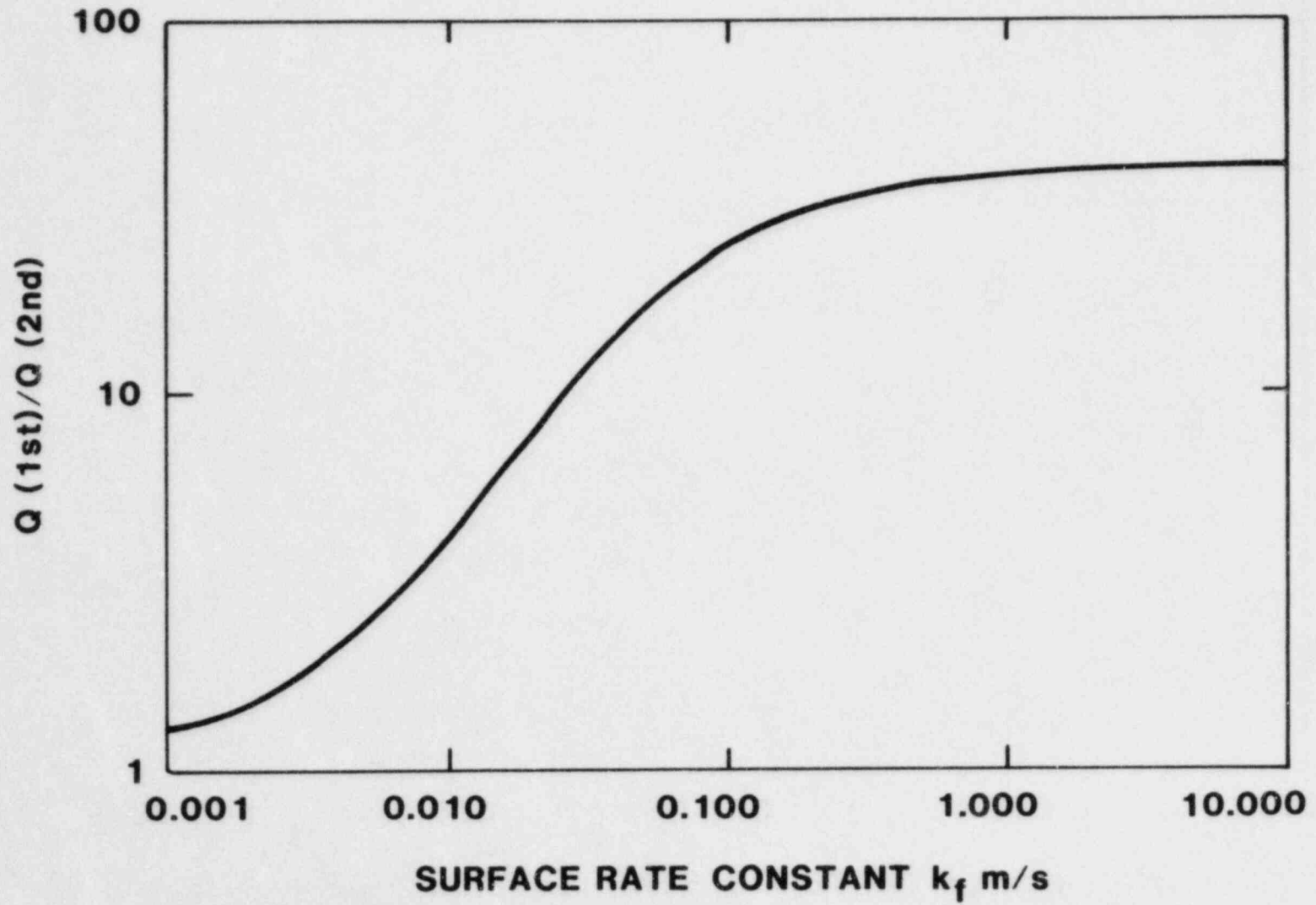


Figure A-2. Effect on  $k_f$  on Deposition Profile



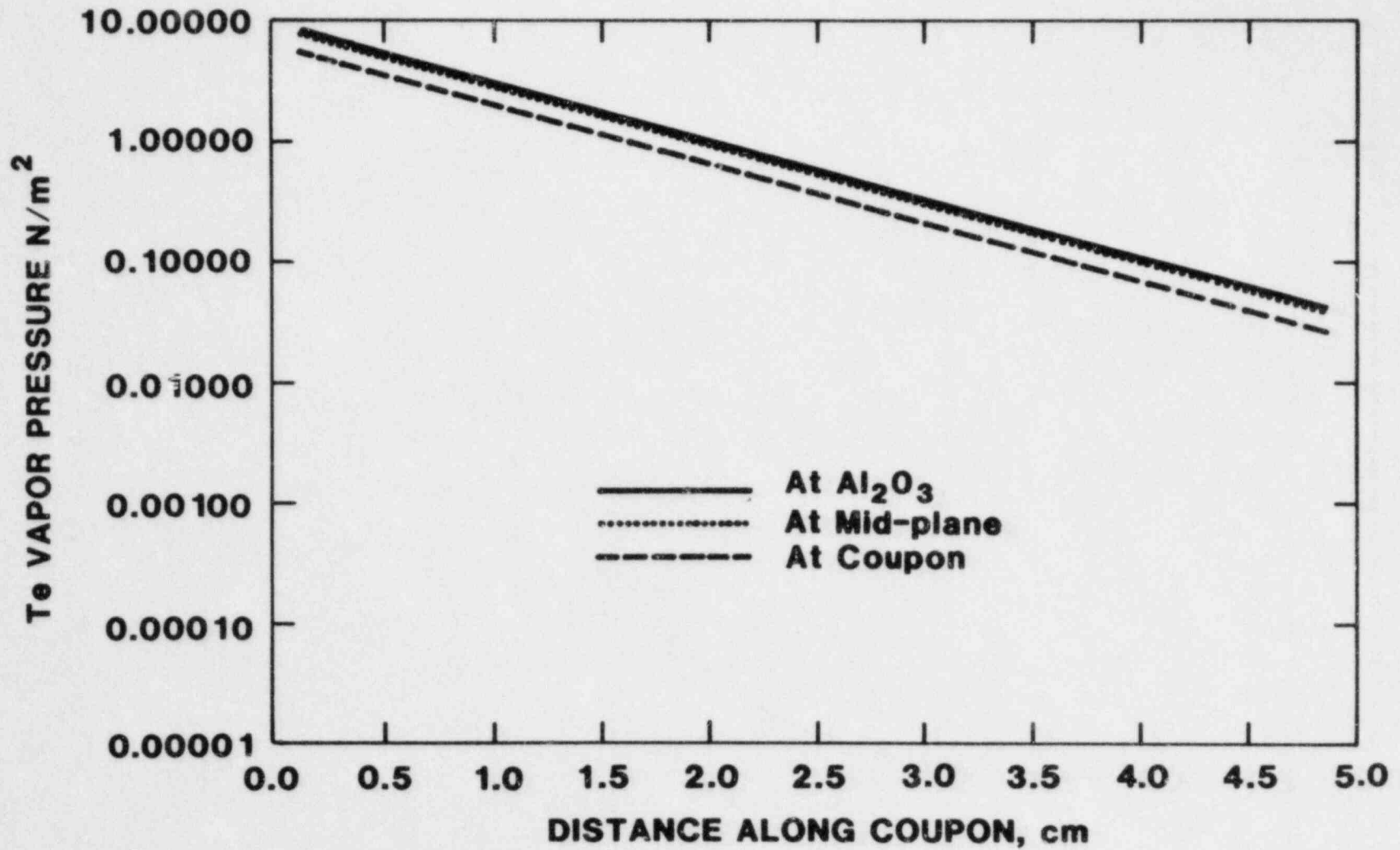


Figure A-3. Axial Vapor Pressure Profiles--Surface Rate Constant = 0.01 m/s



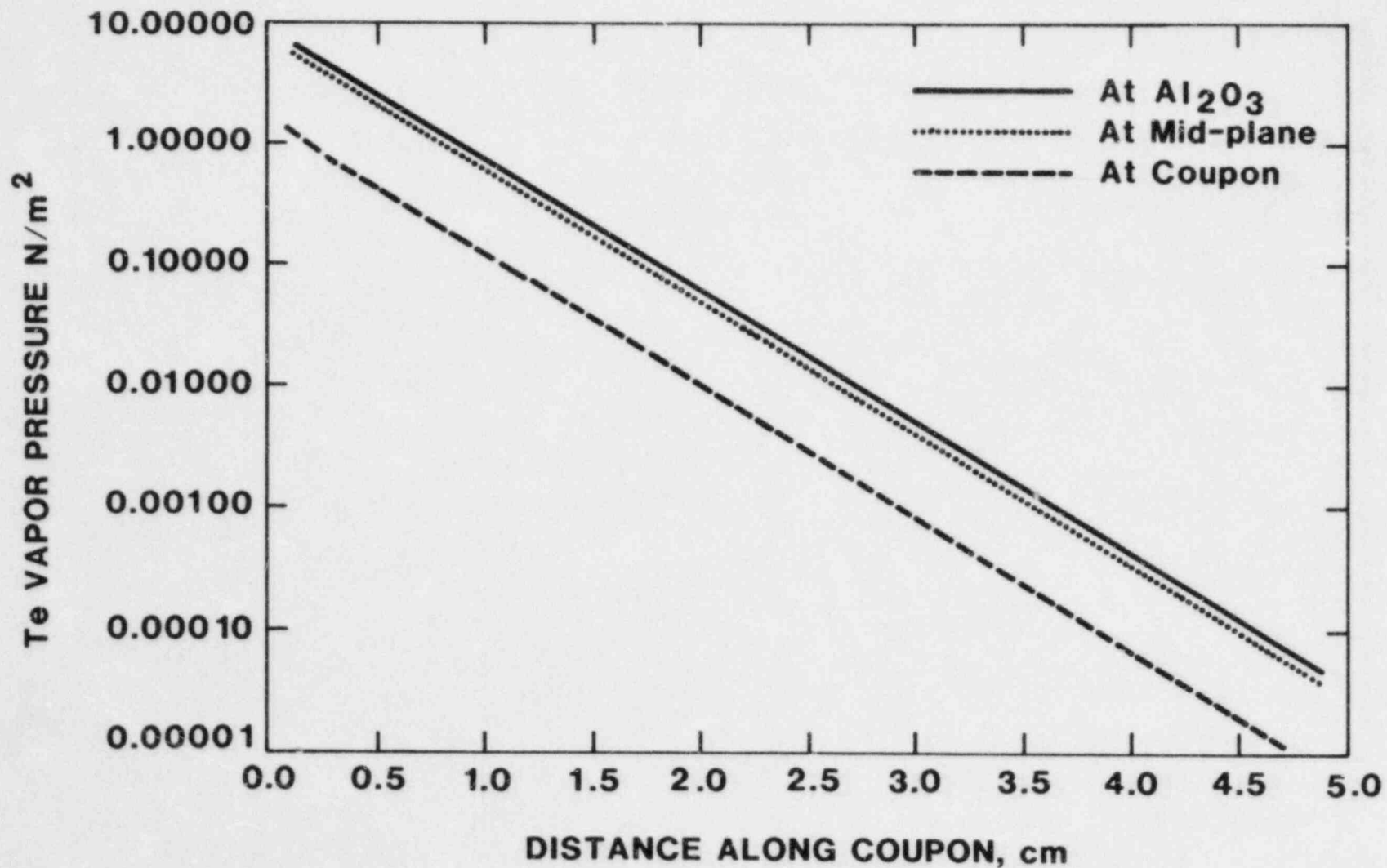


Figure A-4. Axial Vapor Pressure Profiles--Surface Rate Constant = 0.1 m/s

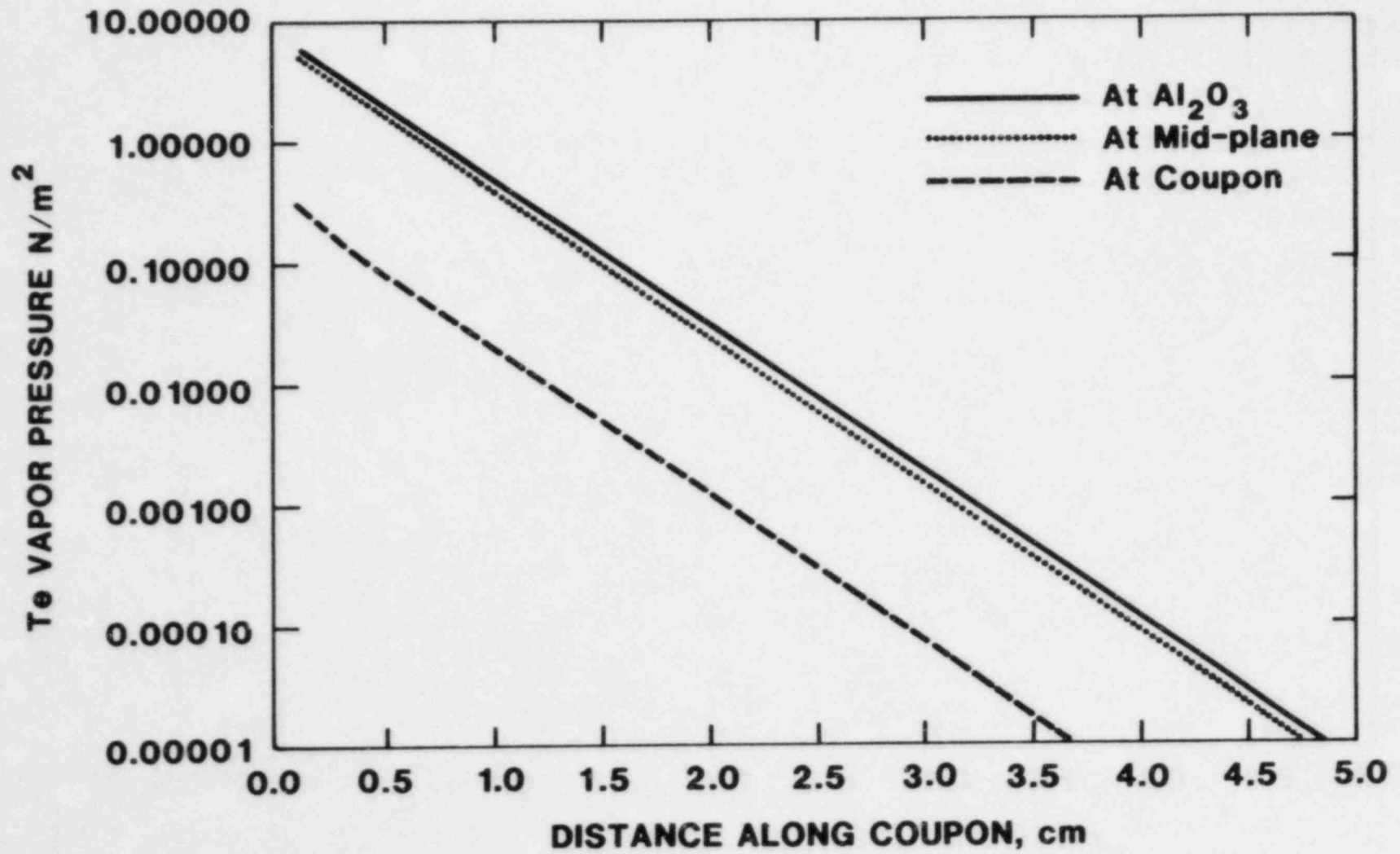


Figure A-5. Axial Vapor Pressure Profiles--Surface Rate Constant = 1.0 m/s

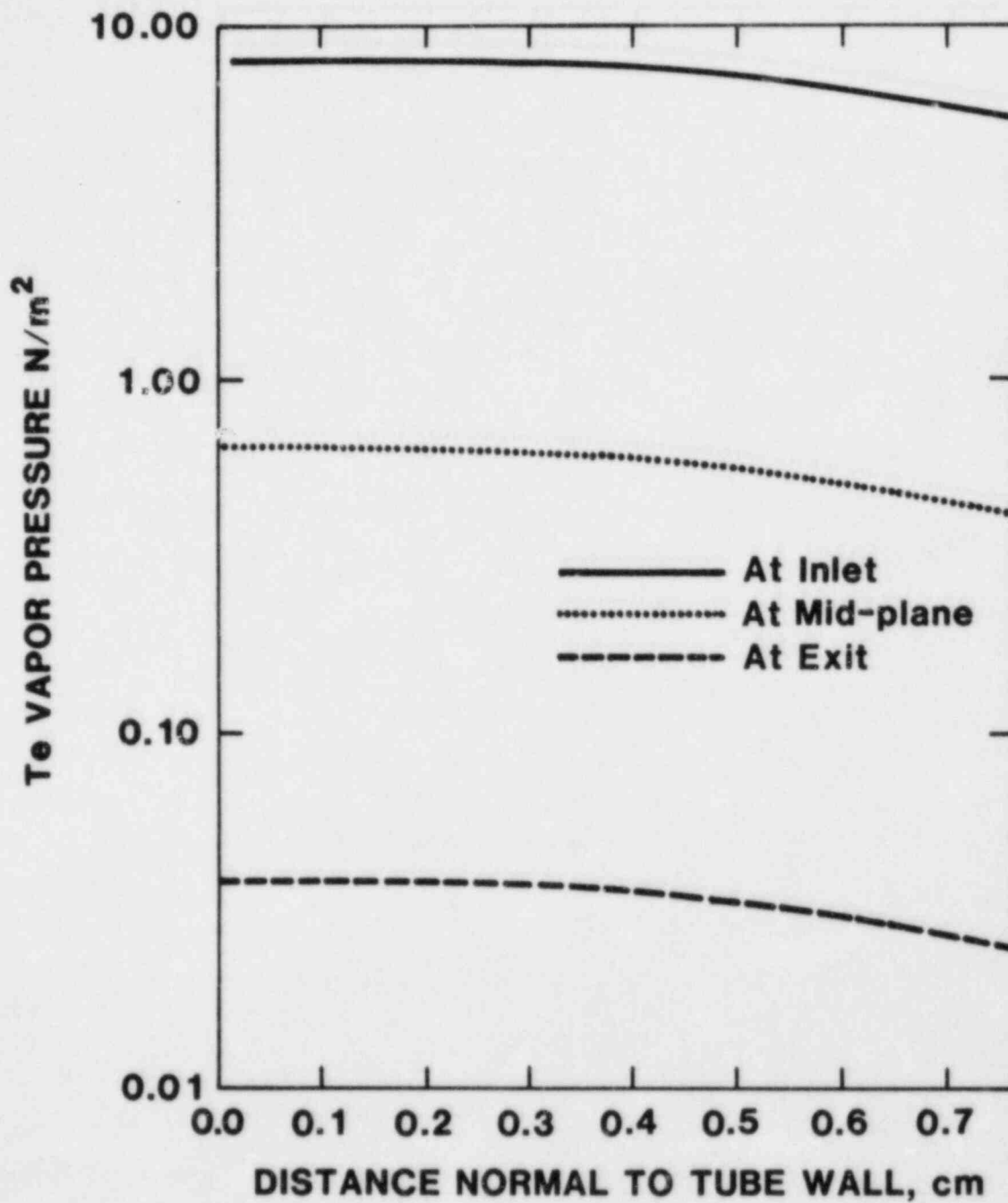


Figure A-6. Radial Vapor Pressure Profiles--  
Surface Rate Constant - 0.01 m/s

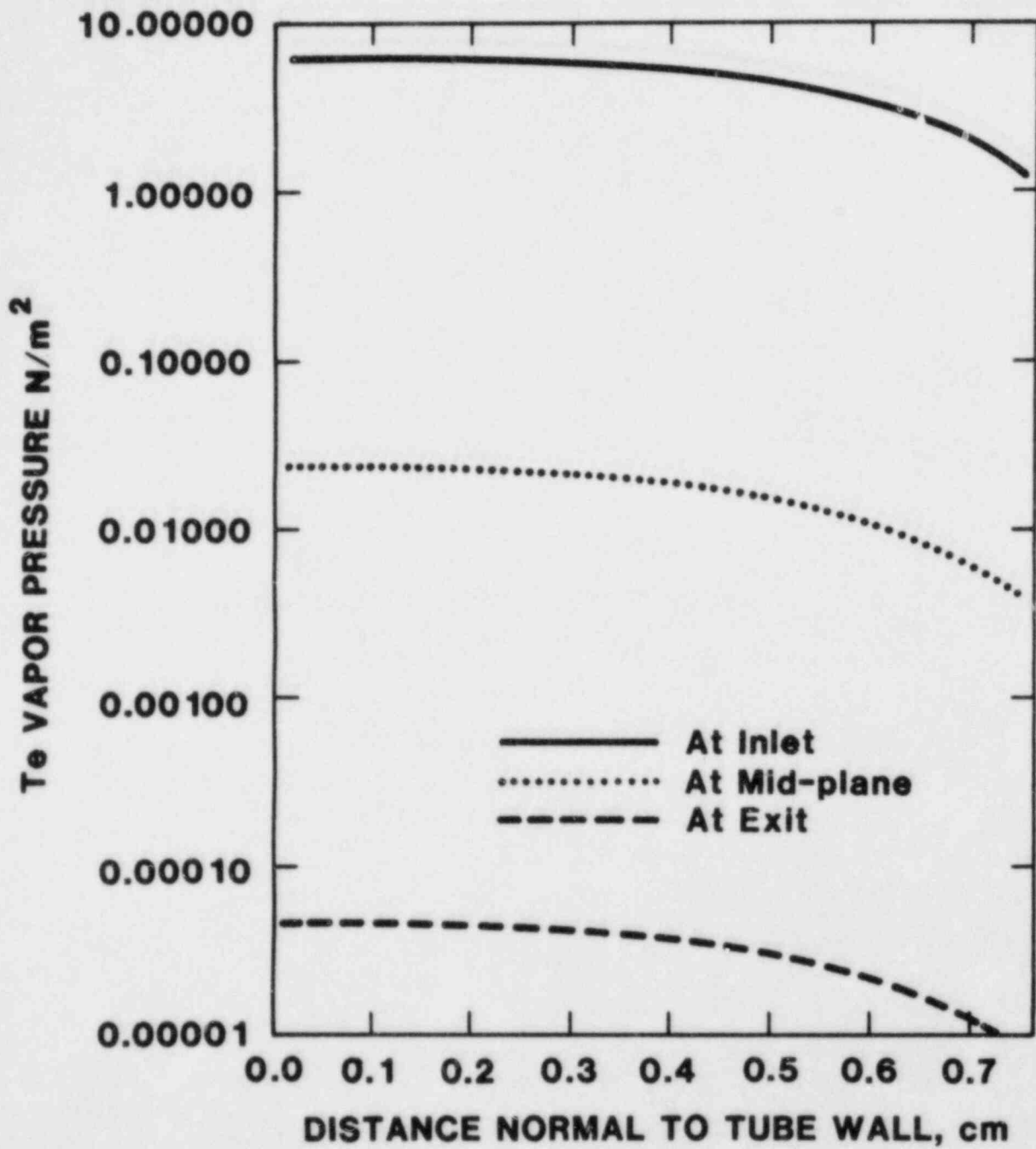


Figure A-7. Radial Vapor Pressure Profiles--  
Surface Rate Constant = 0.1 m/s

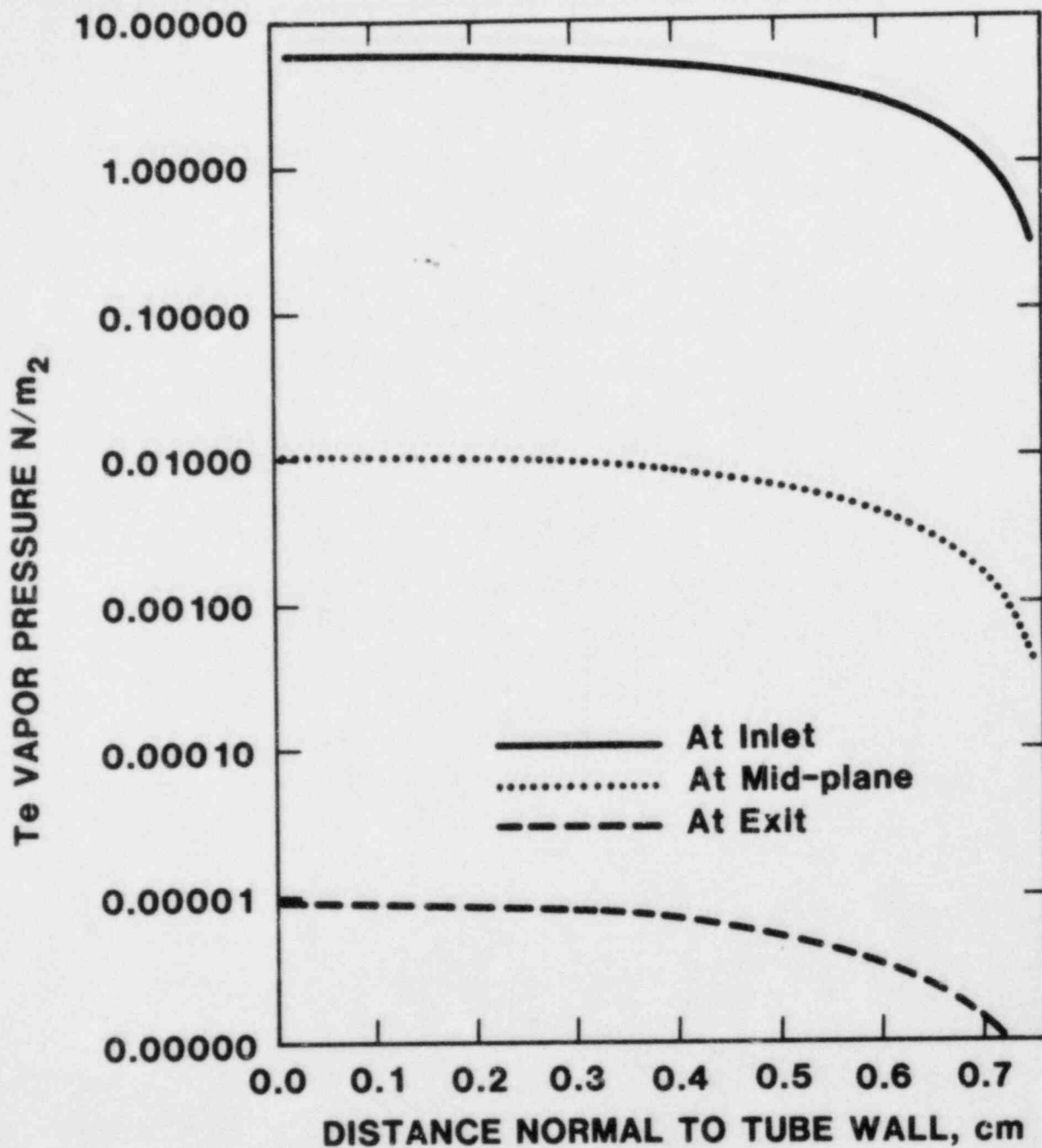


Figure A-8. Radial Vapor Pressure Profiles--  
Surface Rate Constant = 1.0 m/s

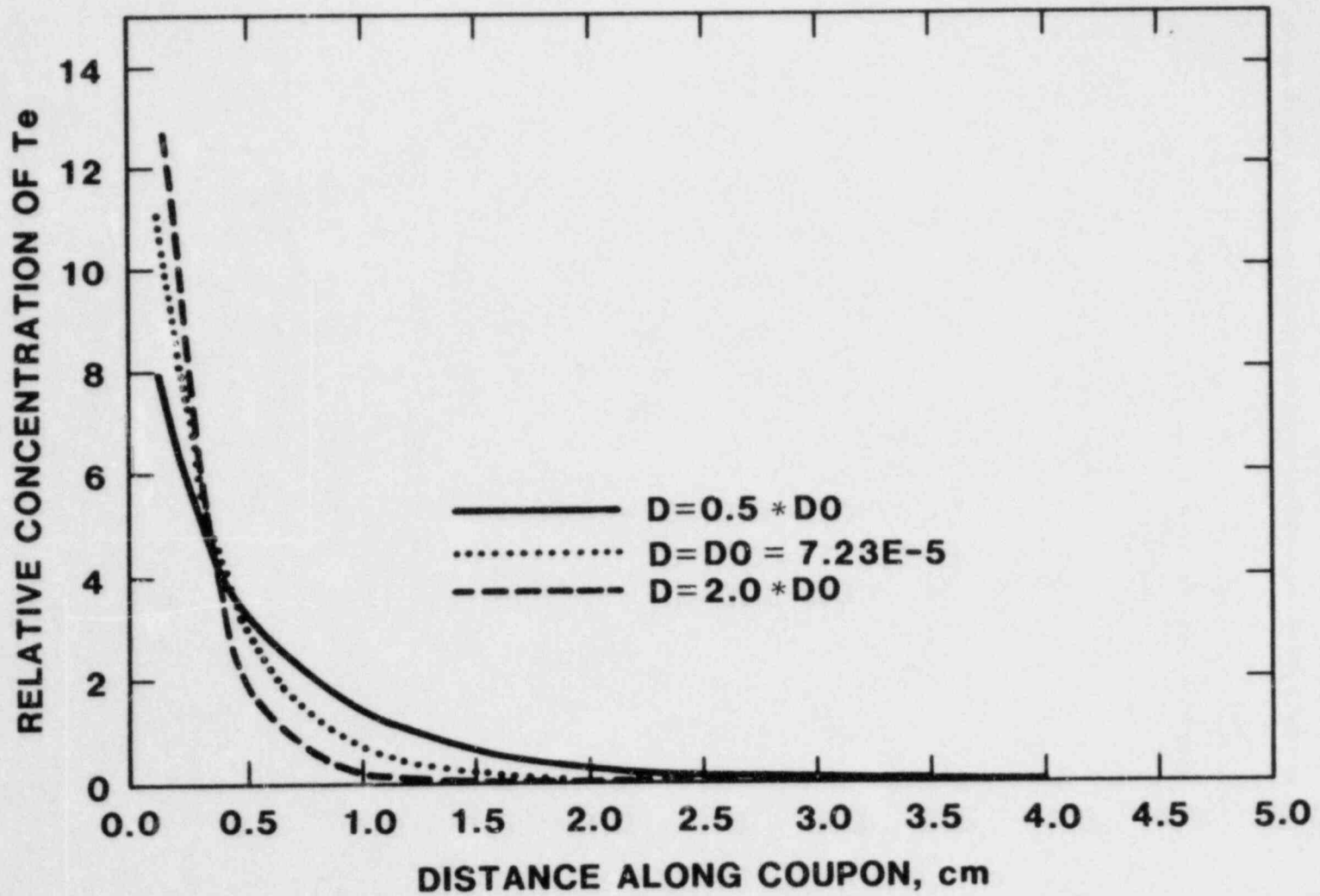


Figure A-9. Effect of Gas Phase Tellurium Diffusion Coefficient on the Mass Transfer Limited Deposition Profiles



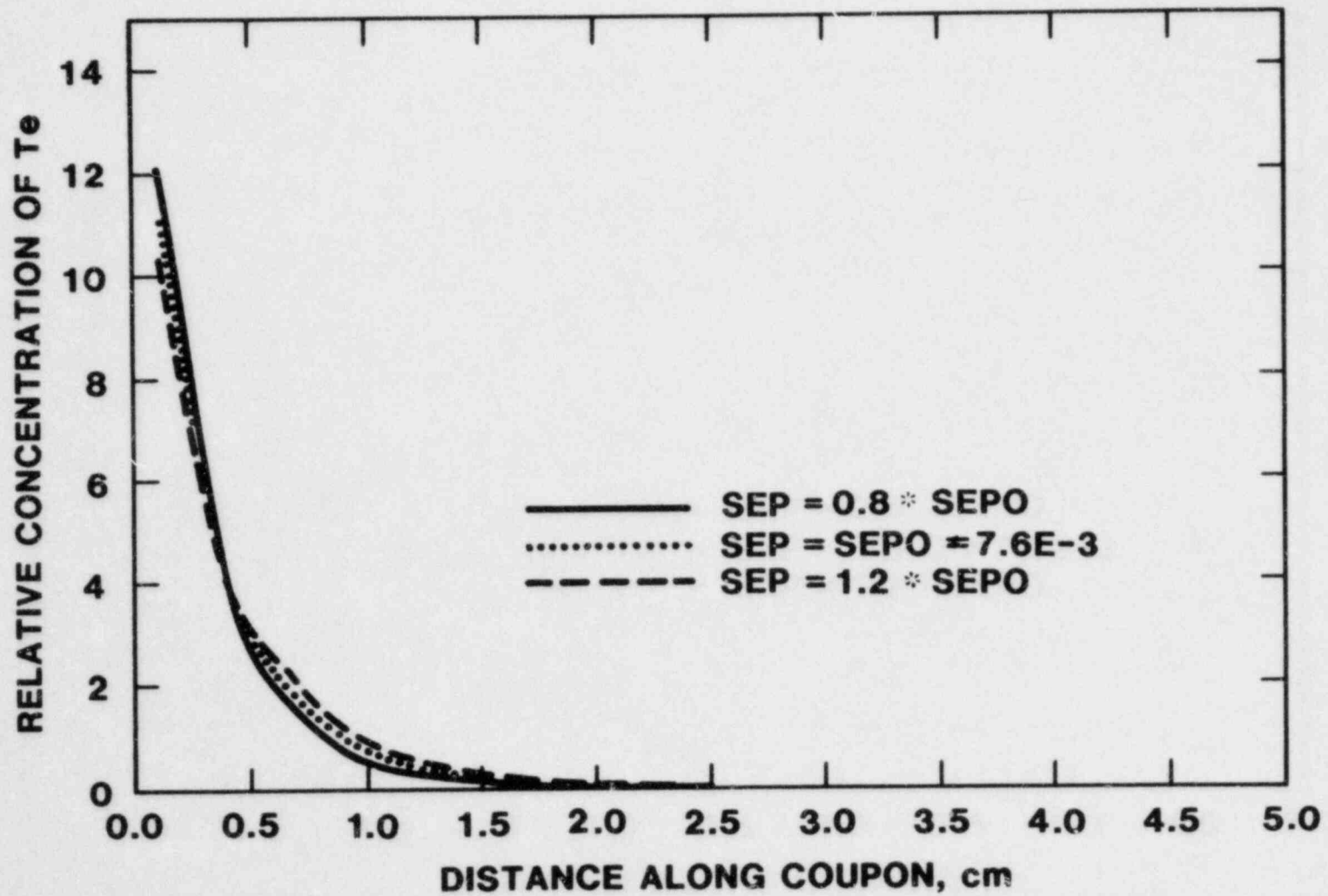


Figure A-10. Effect of Assumed Plate Separation on the Mass Transfer Limited Deposition Profiles

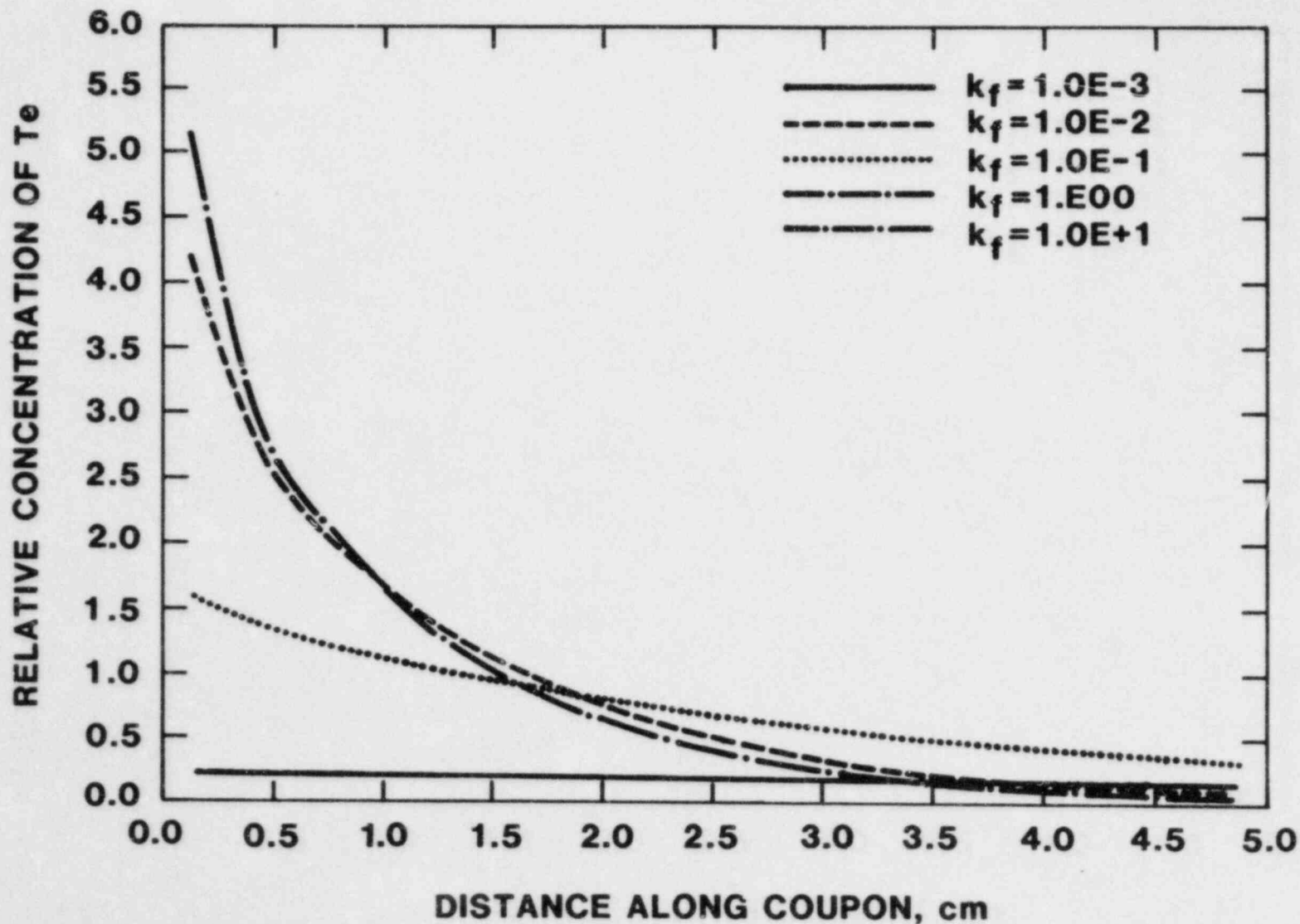


Figure A-11. Tellurium Deposition Profiles Calculated Assuming a Four-Fold Increase in Carrier Gas Flow Rate. Compare to Figure 9 of main text.

the gas flow, and the closeness to a mass-transfer-limited profile of those observed in the experiments, renders any greater precision impossible with the existing data.

2. It seems likely that tellurium vapor deposited on most of the material studied at a rate limited by mass transport through the carrier gas; in any case, it is not possible to deduce a more accurate value for the reaction rate constant of tellurium vapor on the materials studied from the experiments performed to date.

3. The diffusion coefficient of tellurium vapor in argon is an important parameter needed for the interpretation of deposition measurements in terms of surface reaction kinetics. It could be determined with far better accuracy than it may be estimated theoretically in experiments performed in a system more amenable to hydrodynamic analysis (eg, in cylindrical geometry).

4. Repetition of the experiments performed at Sandia at higher carrier gas flow rates, while providing a useful check on the flow modeling performed to date, would not of itself enable estimates of surface reaction kinetics to be refined.

5. If it can be demonstrated (eg, by TRAP-MELT sensitivity studies) that there is a need to refine estimates of surface reaction rate constants more closely than "greater than a few cm/sec," further experiments should be performed in a system with better-defined hydrodynamic properties. Even if this is not the case, further experiments to determine the diffusion coefficient of tellurium vapor in prototypic gases may be needed. In the system analyzed here, a 4-fold change in the diffusion coefficient produced a change of more than 6 orders of magnitude in the fraction of Te vapor transmitted through the system.

## References

- A-1. Trybal, R. E., "Mass Transfer Operations" 2nd ed., McGraw Hill Publ.
- A-2. Taig, A. R., "Advanced Reactor Safety Research Quarterly Report" Jan., March 1982, SAND82-0904 (184); NUREG/CR-2679 (1 of 4).
- A-3. Shampine, L. F., and H. A. Watts, "DEPAC-Design of a User-Oriented Package of ODE Solvers," SAND79-2374, Sandia National Laboratories, 1979.

## Appendix B -- Experimental Data

This appendix contains, in tabulated form, the conditions and results for the tellurium adsorption experiments (Table B-I), the x-ray diffraction data for the reaction products (Table B-II), and the conditions and results for the tellurium desorption experiments (Table B-III).

A microbalance recorder trace from one of the adsorption experiments is shown in Figure B-1 to illustrate the response of the microbalance/furnace system to changes in the temperature of the tellurium reservoir. In figures B-2 through B-7 are reproductions of the x-ray diffraction traces obtained for the various reactor materials studied. From these traces, the data tabulated in Table B-II were derived.

TABLE B-I

## EXPERIMENTAL DATA FOR TELLURIUM ADSORPTION (REACTION)

NICKEL

<u>SAMPLE TEMP, °C</u>	<u><math>10^4/T_{Te}</math></u>	<u>Te PRESS</u>	<u>Te Flow (CALCULATED)</u>	<u>Mass Gain (MEASURED)</u>
760	1.54	.029	.016	.016
760	1.51	.040	.023	.024
760	1.42	.124	.060	.072
760	1.37	.240	.118	.140
760	1.32	.470	.215	.280

304 SS

500	1.49	.050	.029	.024
500	1.44	.100	.060	.074
500	1.36	.260	.151	.180
500	1.33	.390	.230	.270
760	1.44	.090	.054	.059
760	1.38	.200	.116	.120
760	1.31	.520	.301	.280
760	1.29	.720	.418	.470

I-600

480	1.48	.060	.035	.035
480	1.42	.130	.075	.072
480	1.37	.250	.145	.160
500	1.32	.440	.255	.300
785	1.43	.110	.064	.064
785	1.39	.190	.110	.110
785	1.35	.330	.191	.200
785	1.31	.540	.310	.340
490	1.47	.069	.040	.041
490	1.53	.030	.017	.016
490	1.40	.170	.099	.110
800	1.50	.048	.028	.027
800	1.44	.094	.055	.050
800	1.40	.160	.095	.095
800	1.35	.310	.178	.230



TABLE B-I (Cont'd)

## 304 SS (Oxidized)

<u>SAMPLE TEMP, °C</u>	<u>10<sup>4</sup>/K<sub>Te</sub></u>	<u>Te PRESS</u>	<u>Te Flow (CALCULATED)</u>	<u>Mass Gain (MEASURED)</u>
490	1.46	.075	.044	.039
490	1.40	.160	.090	.090
490	1.36	.280	.160	.190
790	1.40	.160	.090	.064
790	1.37	.250	.147	.150
790	1.33	.420	.250	.270
790	1.33	.420	.250	.250

## I-600 (Oxidized)

800	1.39	.170	.099	.100
800	1.40	.070	.044	.043
800	1.50	.040	.024	.026
500	1.50	.040	.024	.026
500	1.50	.040	.024	.022
500	1.49	.049	.029	.029
500	1.43	.110	.064	.068

TABLE B-II

## X-RAY DIFFRACTION DATA FOR TELLURIDE PRODUCTS

<u>Ni</u>		<u>Inconel 600</u>		<u>304 SS</u>	
6.0 (50)	_____	6.0 (10)	_____	6.2 (20)	_____
3.18 (*) <sup>2</sup>	_____	3.18 (100)	_____	3.24 (8)	_____
3.01 (100)	_____	3.01 (20)	_____	3.10 (15)	_____
		2.96 (40)	_____	2.97 (*)	_____
2.66 (*)	_____	2.66 (50)	_____	2.77 (15)	_____
2.43 (100)	_____	2.43 (80)	_____	2.47 (30)	_____
2.36 (15)	_____	2.36 (10)	_____		
		2.25 (10)	_____	2.26 (30)	_____
2.00 (*)	_____	2.00 (*)	_____	2.07 (20)	_____
		1.95 (35)	_____	1.96 (80)	_____
1.89 (90)	_____	1.89 (35)	_____	1.91 (50)	_____
1.78 (20)	_____	1.78 (20)	_____	1.82 (25)	_____
			_____	1.74 (15)	_____
1.62 (40)	_____	1.62 (30)	_____	1.65 (40)	_____
		1.61 (10)	_____	1.61 (30)	_____
1.60 (30)	_____	1.60 (10)	_____		
1.51 (20)	_____	1.51 (10)	_____		
			_____	1.50 (10)	_____
			_____	1.48 (10)	_____
			_____	1.44 (10)	_____
1.38 (30)	_____	1.38 (15)	_____	1.40 (15)	_____
1.33 (30)	_____	1.33 (15)	_____	1.32 (15)	_____
1.30 (10)	_____	1.30 (10)	_____		
		1.24 (10)	_____	1.26 (15)	_____
$\gamma$ (I)		$\gamma$ (I)		$\gamma$ (I)	
	$\text{Ni}_{2.86}\text{Te}_2$ (24-0798) (1)		$\text{CrTe}$ (26-0442)		$\text{Fe}_{2.25}\text{Te}_2$ (29-0729)

1) Figures in parentheses under formulas indicate x-ray pattern number (Ref. 10).

2) Asterisk in intensity location denotes off scale reading ( 100).

3) M denotes diffraction line of base metal.

TABLE B-II (cont'd)

Oxidized I-600

<u>Zircaloy-2</u>		<u>Leading</u>		<u>Trailing</u>	
3.67 (5)		5.37 (10)			
3.62 (5)		3.64 (10)	_____	3.64 (20)	
3.40 (5)	_____	3.33 (25)		3.20 (30)	_____
3.30 (5)				3.02 (10)	_____
3.15 (20)	_____	2.81 (*)		2.88 (*)	
3.02 (100)	_____	2.66 (15)	_____	2.66 (50)	
2.83 (15)	_____	2.63 (30)		2.54 (15)	
2.61 (10)		2.48 (20)	_____	2.48 (40)	
2.37 (25)	_____			2.44 (10)	_____
1.97 (*)	_____	2.17 (10)	_____	2.17 (15)	
1.85 (10)	_____	2.07			
1.81 (10)		2.05 (*)	M <sup>(3)</sup>	2.05 (*)	
1.69 (10)				2.00 (30)	_____
1.65 (35)	_____	1.9 (80)		1.98 (30)	
1.52 (10)	_____	1.81 (10)	_____	1.81 (10)	
1.47 (5)	_____	1.77 (*)	M	1.77 (*)	
1.35 (5)	_____	1.67 (15)	_____	1.67 (20)	
1.27 (30)	_____			1.63 (20)	
		1.59 (50)		1.59 (20)	
		1.47 (10)	_____	1.47 (10)	
		1.41 (20)			
		1.32 (5)		1.34 (5)	
		1.26 (*)	M	1.26 (*)	

(ZrTe)  
(15-0223)

NiTe<sub>2</sub>  
(8-004)

Cr<sub>2</sub>O<sub>3</sub>  
(6-0504)  
M=metal

Ni<sub>2.86</sub>Te<sub>2</sub>  
(24-0798)

TABLE B-II (cont'd)

Oxidized 304 SS

_____	4.84 (10)	_____
	4.01 (10)	
	3.62 (5)	
_____	3.28 (40)	
_____	3.11 (35)	
	2.97 (25)	_____
	2.85 (60)	
_____	2.78 (*)	
_____	2.68 (*)	
_____	2.63 (30)	
	2.53 (50)	_____
	2.42 (10)	_____
_____	2.12 (20)	
	2.06 (90)	
_____	2.05 (75)	
_____	2.01 (10)	
_____	1.93 (30)	
_____	1.83 (40)	
_____	1.79 (35)	
_____	1.73 (20)	
_____	1.69 (5)	
_____	1.61 (15)	_____

FeFe<sub>2</sub>  
(7-0367)

Fe<sub>3</sub>O<sub>4</sub>

TABLE B-III

## DATA FOR TELLURIUM DESORPTION EXPERIMENTS

## Ni(Te) Solid Solution

<u>T(c)</u>	<u>10<sup>4</sup>/T(K)</u>	<u>10<sup>4</sup>RI</u>
837	9.01	.74
892	8.58	2.30
920	8.38	4.70
841	8.98	.98
951	8.17	7.10
884	8.64	3.80
967	8.06	8.00
903	8.50	3.60
936	8.27	5.30
977	8.00	11.00

## 304 SS(Te) Solid Solution

<u>T(C)</u>	<u>10<sup>4</sup>/T(K)</u>	<u>10<sup>4</sup>R*</u>
829	9.07	1.00
878	8.69	.74
921	8.38	1.85
987	7.94	19.50
878	8.69	3.30
959	8.12	4.80
950	8.26	2.40
824	9.12	.66
876	8.70	1.80
903	8.53	2.60
824	9.12	.53
928	8.33	5.00
956	8.14	6.30

\*Units of R: Mg/cm<sup>2</sup>-sec

\*The data were obtained using the apparatus sketched in Figure 1b. The nominal flow of argon past the samples was 0.05 liter/minute (640 torr and 20°C). The average gas velocity in the apparatus at the sample location ranged between 0.5 and 1.0 cm/sec.

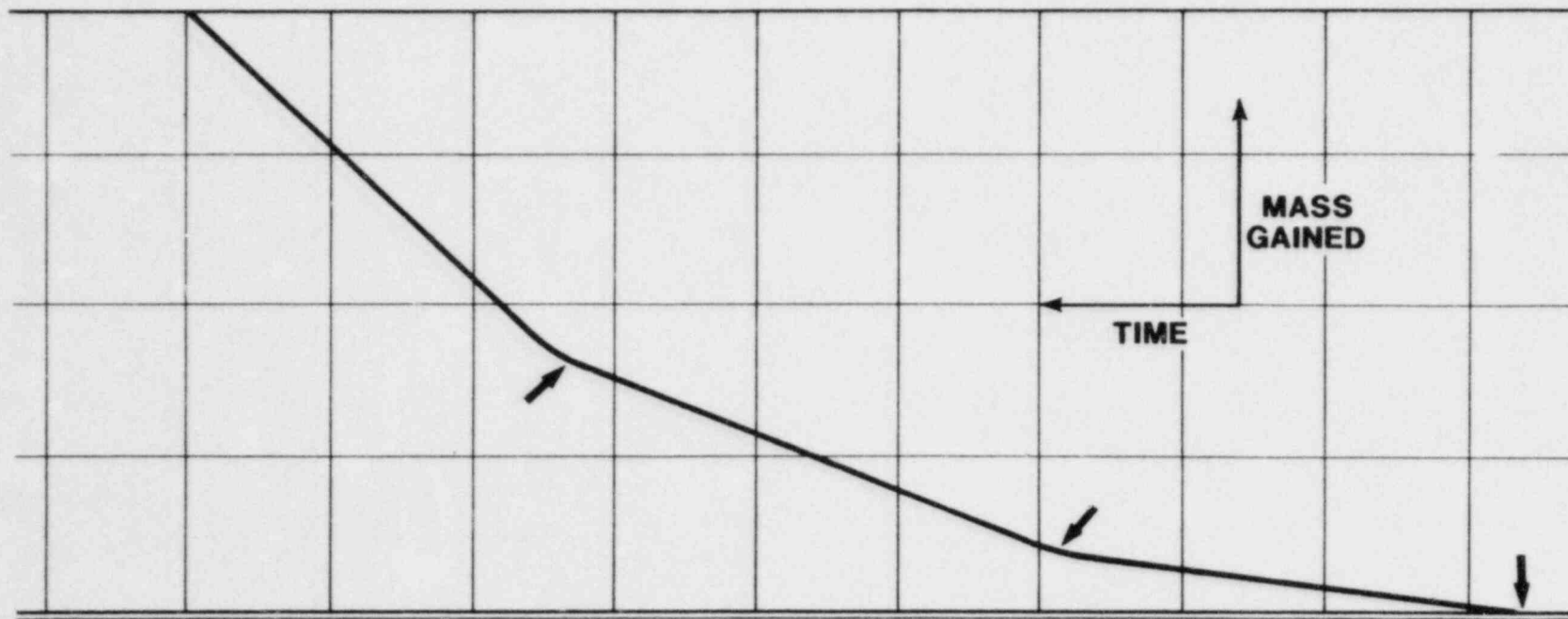


Figure B-1. Recorder Trace of a Microbalance Experiment. The temperature of the tellurium reservoir was increased at the times indicated by the arrows.



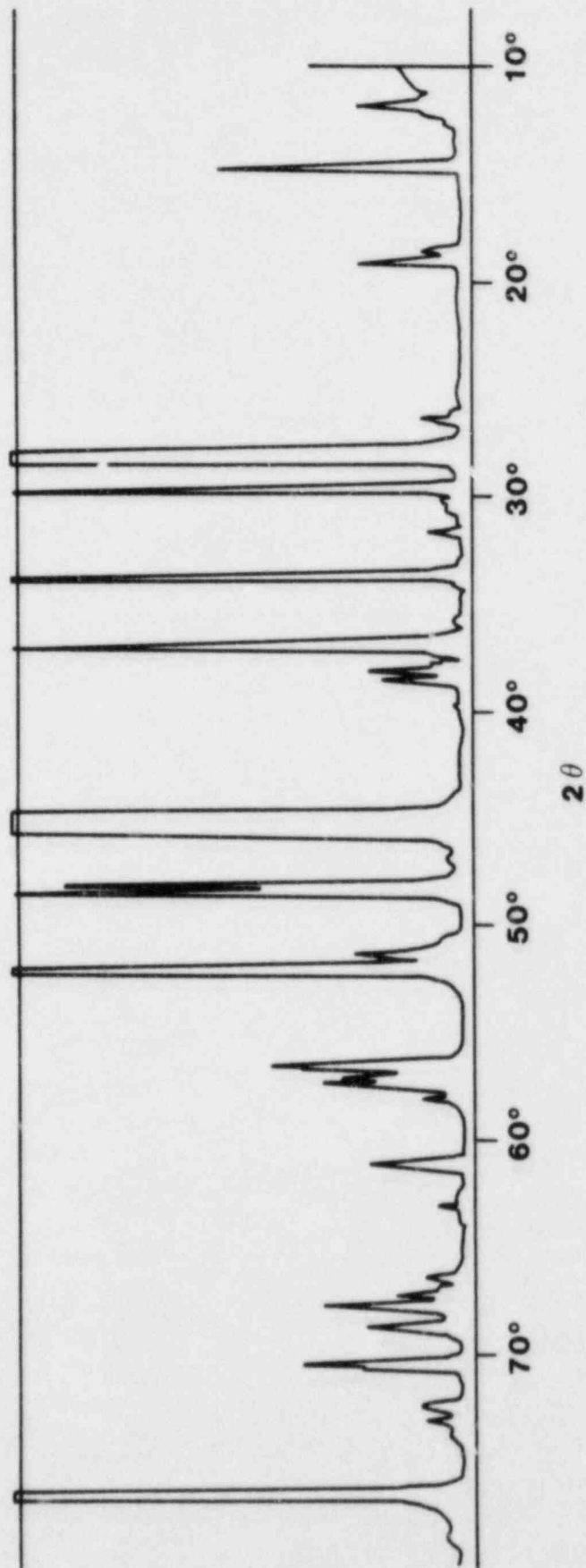


Figure B-2. X-Ray Diffraction Pattern for Tellurium/Nickel Reaction Product

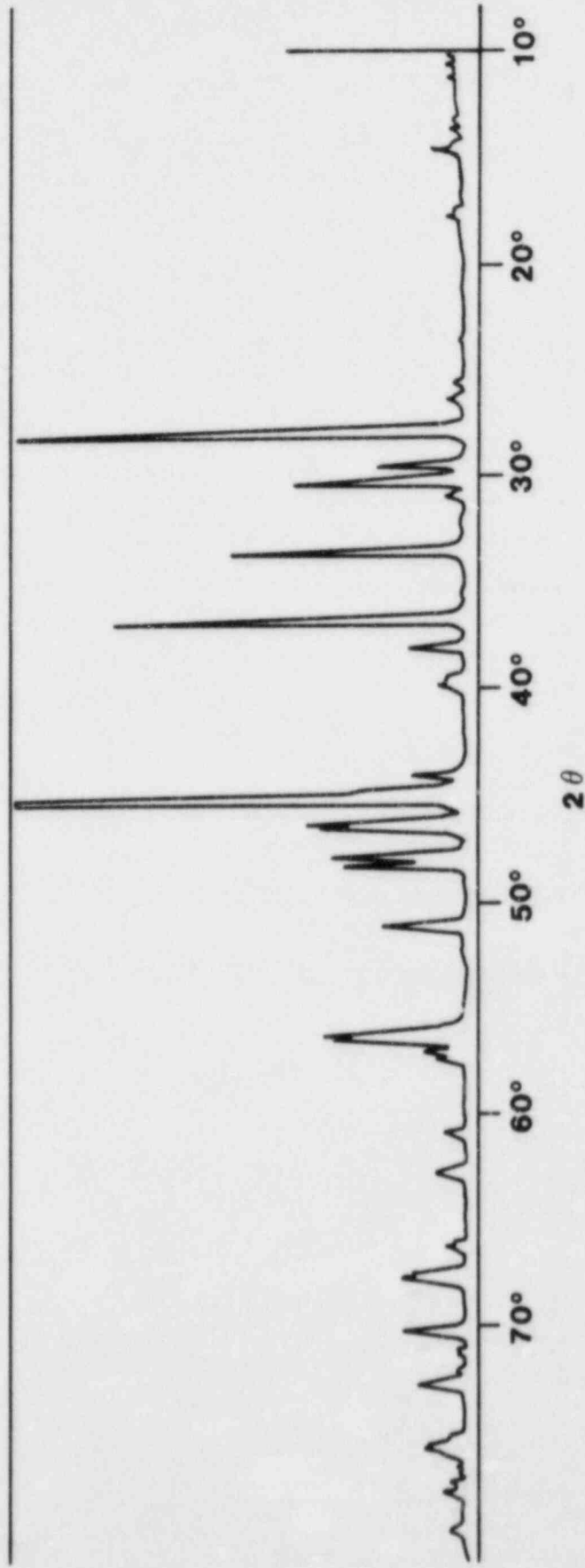


Figure B-3. X-Ray Diffraction Pattern for Tellurium/  
Inconel-600 Reaction Product

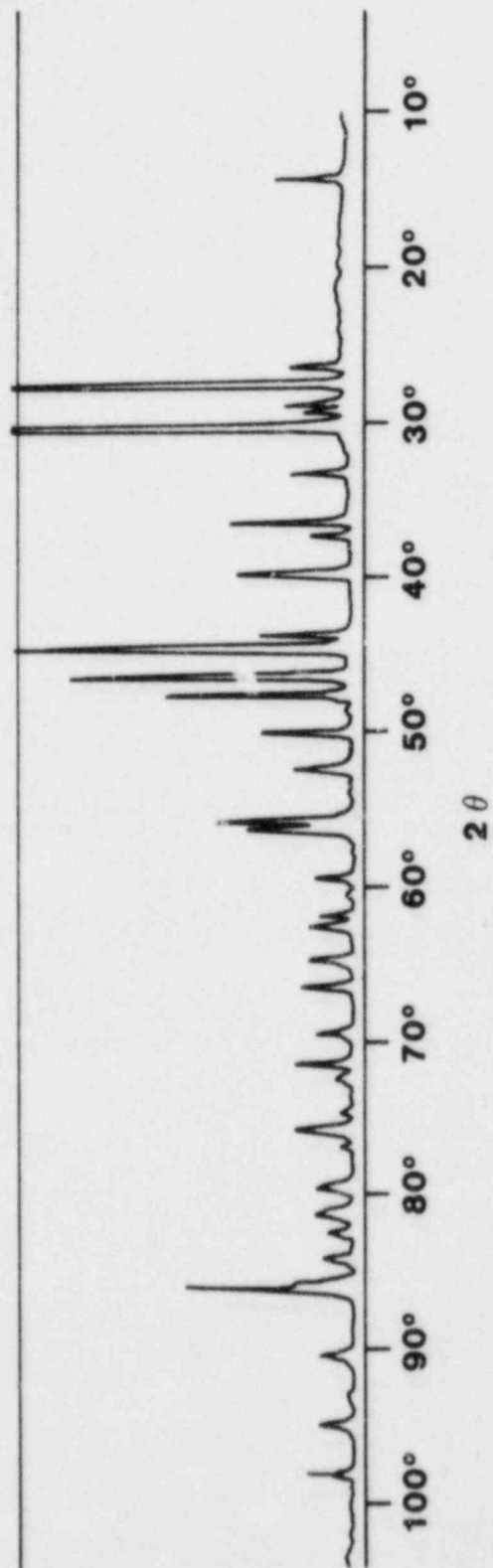


Figure B-4. X-Ray Diffraction Pattern for Tellurium/  
304 Stainless Steel Reaction Product

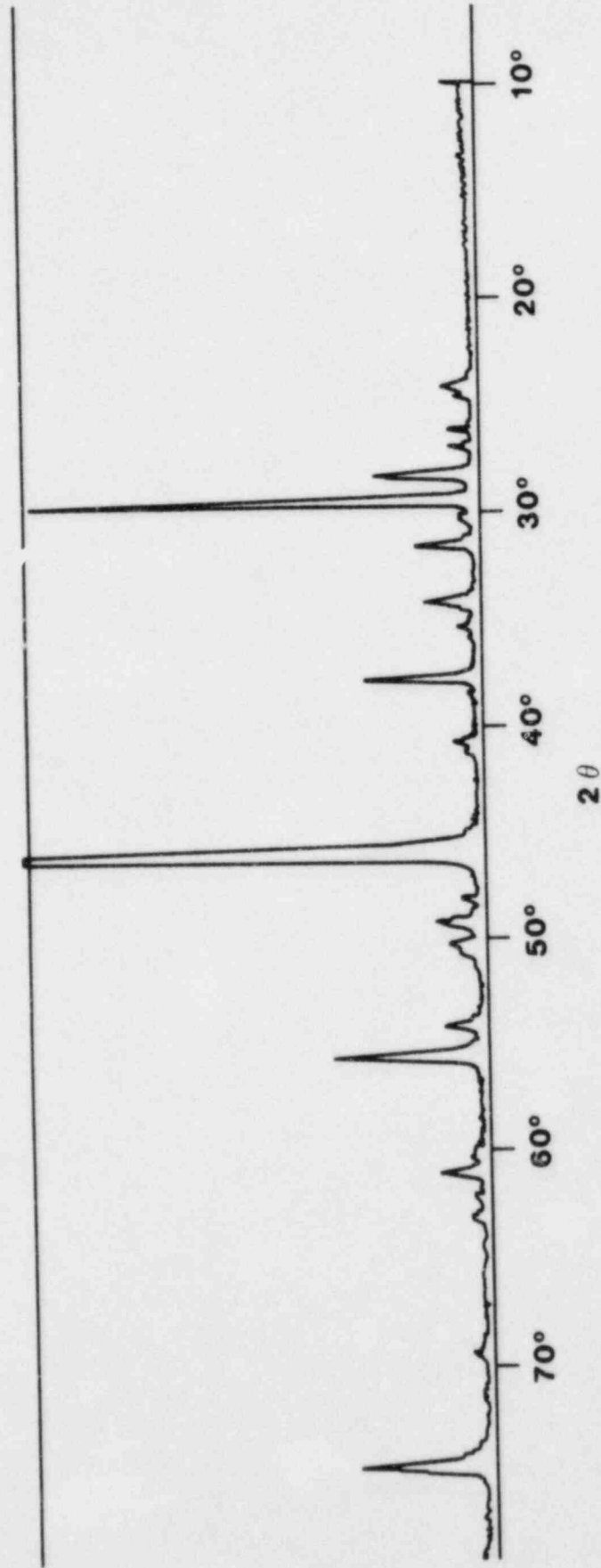


Figure B-5. X-Ray Diffraction Pattern for Tellurium/  
Zircaloy-2 Reaction Product

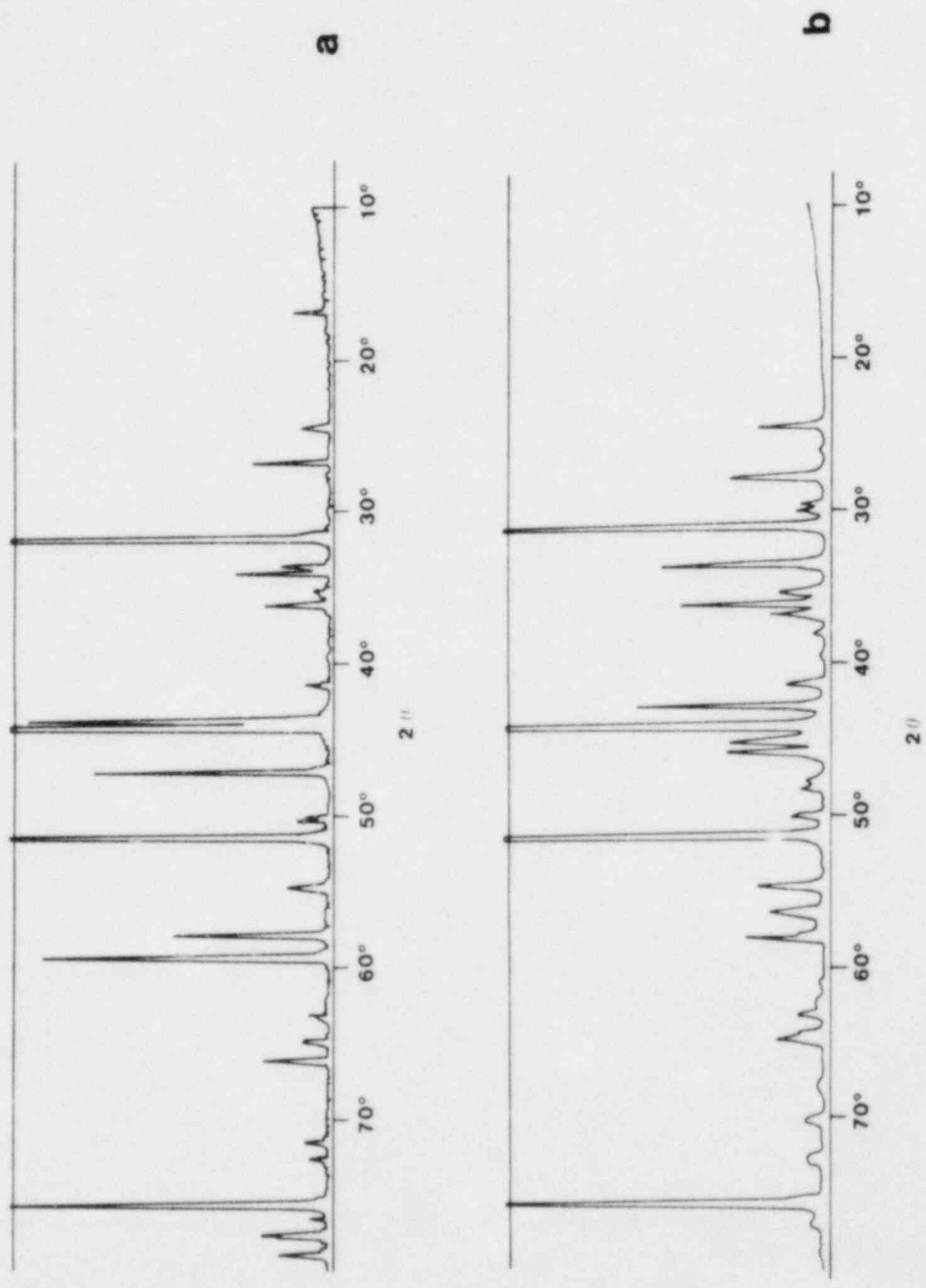


Figure B-6. X-Ray Diffraction Patterns for Tellurium/Oxidized Inconel-600 Reaction Product  
 a) Leading Edge. b) Trailing Edge.

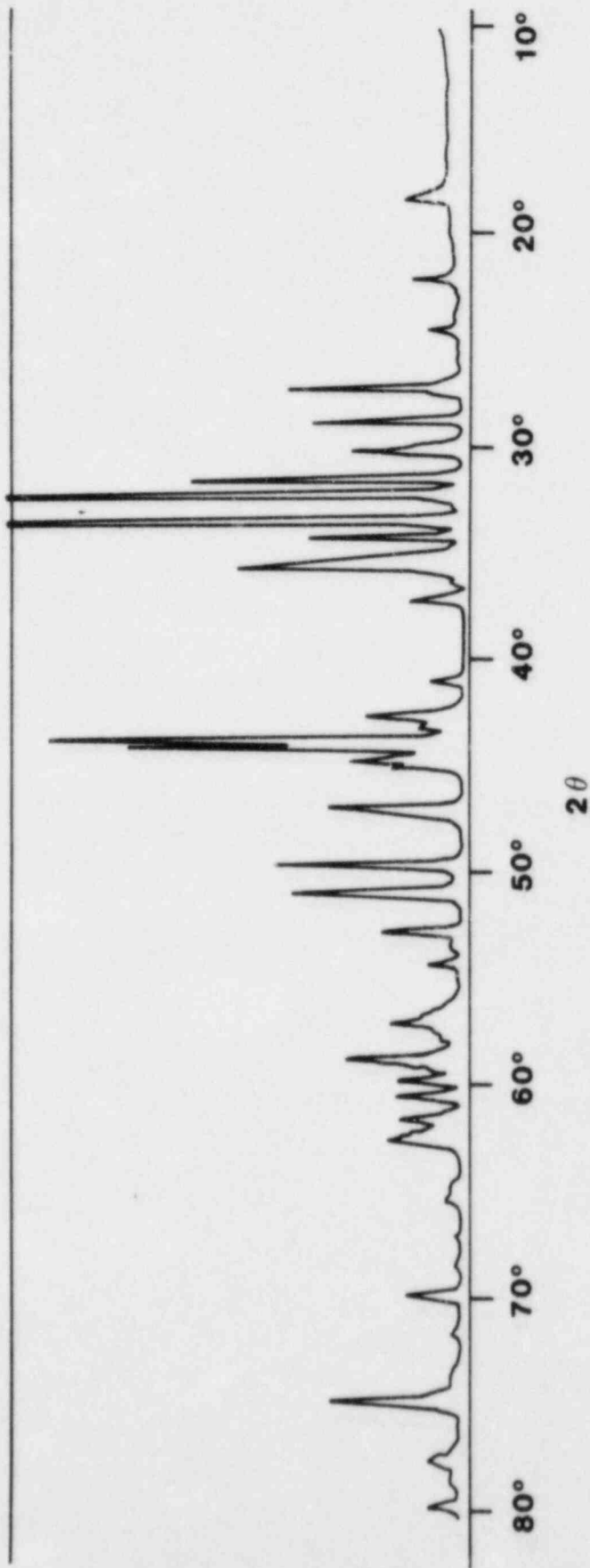


Figure B-7. X-ray Diffraction Pattern for Tellurium/  
Oxidized 304 Stainless Steel Reaction Product



DISTRIBUTION:

U.S. NRC Distribution Contractor (CDSI) (365 copies)  
7300 Pearl Street  
Bethesda, MD 20014  
340 copies for R3  
25 copies for NTIS

U.S. Nuclear Regulatory Commission (16)  
Office of Nuclear Regulatory Research  
Washington, DC 20555  
Attn: O. E. Bassett  
B. S. Burson  
R. T. Curtis  
C. N. Kelber  
J. Larkins  
G. Marino  
L. Chan (5)  
M. Silberberg  
M. Jankowski  
R. W. Wright  
T. Walker  
W. Pasedag

U.S. Nuclear Regulatory Commission (4)  
Office of Nuclear Regulatory Regulation  
Washington, DC 20555  
Attn: L. G. Hulman  
P. Easky  
J. Rosenthal  
J. Mitchell

U.S. Department of Energy (2)  
Albuquerque Operations Office  
P. O. Box 5400  
Albuquerque, NM 87185  
Attn: J. R. Roeder, Director  
Operational Safety Division  
D. K. Nowlin, Director  
Special Programs Division  
For: C. B. Quinn  
D. Plymale

U.S. Department of Energy  
Office of Nuclear Safety Coordination  
Washington, DC 20545  
Attn: R. W. Barber

Electric Power Research Institute  
3412 Hillview Avenue  
Palo Alto, CA 94303  
Attn: R. Vogel

Brookhaven National Laboratory (3)  
Upton, NY 11973  
Attn: R. A. Bari  
T. Pratt  
G. Greene

Professor R. Seale  
Department of Nuclear Engineering  
University of Arizona  
Tucson, AZ

Oak Ridge National Laboratory (5)  
Oak Ridge, TN  
Attn: T. Kress  
R. Wichner  
R. Lorenz  
G. Parker  
R. Spencer

K. Holtzclaw  
General Electric - San Jose  
Mail Code 682  
175 Kurtner Avenue  
San Jose, CA 95125

Argonne National Laboratory  
9700 S. Cass Avenue  
Argonne, IL 60439  
Attn: J. Rest

Cathy Anderson  
Nuclear Safety Oversight Commission  
1133 15th St., NW  
Room 307  
Washington, DC 20005

Battelle Columbus Laboratory (3)  
505 King Avenue  
Columbus, OH 43201  
Attn: P. Cybulskis  
R. Denning  
J. Gieseke

J. E. Antill  
Berkeley Nuclear Laboratory  
Berkeley GL 139 PB  
Gloucestershire  
United Kingdom

W. G. Cunliffe  
Bldg. 396  
British Nuclear Fuels, Ltd.  
Springfields Works  
Salwick, Preston  
Lancs  
United Kingdom

H. J. Teague (3)  
UKAEA  
Safety and Reliability Directorate  
Wigshaw Lane  
Culcheth  
Warrington, WA3 4NE  
United Kingdom

Dr. Fran Reusenbach  
Gesellschaft fur Reaktorsicherheit (GRS mbH)  
Postfach 101650  
Glockengasse 2  
5000 Koeln 1  
Federal Republic of Germany

1830 M. J. Davis  
1840 R. J. Eagan  
1846 R. K. Quinn  
1846 R. A. Sallach (5)  
3141 C. M. Ostrander (5)  
3151 W. L. Garner (3)  
6000 E. H. Beckner  
6400 A. W. Snyder  
6410 D. J. McCloskey  
6412 J. W. Hickman  
6420 J. V. Walker  
6420 J. B. Rivard  
6421 T. R. Schmidt  
6422 D. A. Powers (5)  
6422 J. E. Brockmann  
6422 R. M. Elrick (5)  
6422 E. Copus  
6422 J. E. Gronager  
6423 P. S. Pickard  
6425 W. J. Camp  
6425 M. Pilch  
6427 M. Berman  
6440 D. A. Dahlgren  
6442 W. A. Von Rieseemann  
6449 K. D. Bergeron  
6450 J. A. Reuscher  
6454 G. L. Cano  
7530 T. B. Lane  
7537 N. R. Keltner  
8424 M. A. Pound

Reactor Development Division (4)  
UKAEA - Atomic Energy Establishment  
Winfrith, Dorchester  
Dorset  
United Kingdom  
Attn: R. G. Tyror, Head  
T. Briggs  
R. Potter  
A. Nichols

Projekt Nucleare Sicherheit (3)  
Kerforschungszentrum Karlsruhe  
Postfach 3640  
75 Karlsruhe  
Federal Republic of Germany  
Attn: J. P. Hoseman  
Albrecht  
H. H. Rininsland

Mr. G. Petrangeli  
Direzione Centrale della Sicurezza  
Nucleare e della Protezione Sanitaria (DISP)  
Ente Nazionale Energie Alternative (ENEA)  
Viale Regina Margherita, 125  
Casella Postale N. 2358  
I-00100 Roma A.D., ITALY

Dr. K. J. Brinkman  
Reactor Centrum Nederland  
P.O. Box 1  
1755 ZG Petten  
THE NETHERLANDS

Mr. H. Bairiot, Chief  
Department LWR Fuel  
Belgonucleaire  
Rue de Champde Mars. 25  
B-1050 BRUSSELS, BELGIUM

Dr. S. Saito  
Japan Atomic Energy Research Institute  
Takai Research Establishment  
Tokai-Mura, Naku-Gun  
Ibaraki-ken  
JAPAN

Wang Lu  
TVA  
400 Commerce, W9C157-CK  
Knoxville, TN 37902

M. Fontana  
Director, IDCOR Program  
Technology for Energy, Inc.  
P. O. Box 22996  
10770 Dutchtown Rd.  
Knoxville, TN 37922

